Implications of weak-link behavior on the performance of Mo/Au bilayer transition-edge sensors

Stephen J. Smith, Joseph S. Adams, Catherine N. Bailey, Simon R. Bandler, Sarah E. Busch, James A. Chervenak, Megan E. Eckart, Fred M. Finkbeiner, Caroline A. Kilbourne, Richard L. Kelley, Sang-Jun Lee, Jan-Patrick Porst, Frederick S. Porter, and John E. Sadleir

Citation: Journal of Applied Physics **114**, 074513 (2013); doi: 10.1063/1.4818917
View online: http://dx.doi.org/10.1063/1.4818917
View Table of Contents: http://scitation.aip.org/content/aip/journal/jap/114/7?ver=pdfcov
Published by the AIP Publishing

Implications of weak-link behavior on the performance of Mo/Au bilayer transition-edge sensors

Stephen J. Smith,[1,2] Joseph S. Adams,[1,2] Catherine N. Bailey,[3] Simon R. Bandler,[1,4] Sarah E. Busch,[3] James A. Chervenak,[1] Megan E. Eckart,[1,2] Fred M. Finkbeiner,[1,5] Caroline A. Kilbourne,[1] Richard L. Kelley,[1] Sang-Jun Lee,[3] Jan-Patrick Porst,[1,6] Frederick S. Porter,[1] and John E. Sadleir[1]
[1]*NASA Goddard Space Flight Center, Greenbelt, Maryland 20771, USA*
[2]*CRESST and University of Maryland Baltimore County, Maryland 21250, USA*
[3]*NASA Postdoctoral Program Fellow, Goddard Space Flight Center, Greenbelt, Maryland 20771, USA*
[4]*CRESST and University of Maryland College Park, Maryland 20742, USA*
[5]*Wyle Information Systems, McLean, Virginia 22102, USA*
[6]*CRESST and USRA, 10211 Wincopin Circle, Columbia, Maryland 21044, USA*

(Received 7 May 2013; accepted 5 August 2013; published online 21 August 2013)

Understanding the physical properties of the superconducting-to-normal transition is fundamental for optimizing the design and performance of transition-edge sensors (TESs). Recent critical current I_C measurements of square Mo/Au bilayer structures show that they act as weak superconducting links, exhibiting oscillatory, Fraunhofer-like behavior with applied magnetic field. In this paper, we investigate the implications of this behavior for TES x-ray detectors operated in the resistive transition. These devices include normal metal features used for absorber attachment and suppression of detector noise. We present extensive measurements of I_C as a function of temperature T and field B, which show a complex temperature and current evolution when compared with the behavior expected from a simple geometry. We introduce a resistively shunted junction model for describing the TES resistive transition as a function of current I, temperature T, and magnetic field B. From this model, we calculate the $R(T,I,B)$ transition and the logarithmic resistance sensitivity with respect to T and I (α and β, respectively), as a function of applied magnetic field and operating point within the resistive transition. Different examples are presented to illustrate the role of critical current on the transition parameters, and results are qualitatively compared with measurements. Results show that the important device parameters α and β exhibit oscillatory behavior with applied magnetic field due to the modulation of the critical current. This in turn affects the signal responsivity and noise, and the predicted energy resolution. These results show the significance of the critical current in determining the performance of TESs and how externally applied and self-induced magnetic fields can affect the transition and, thus, hold promise for future optimization. © *2013 AIP Publishing LLC*. [http://dx.doi.org/10.1063/1.4818917]

I. INTRODUCTION

Transition-edge sensor (TES) microcalorimeters[1] are under development by numerous groups worldwide for a variety of ground based and space based applications in photon and particle spectroscopy.[2–8] We are currently pursuing high fill-factor, high quantum efficiency, kilo-pixel arrays of TESs for a variety of applications in x-ray spectroscopy.[9–13] Our typical arrays are designed to achieve full-width-at-half-maximum (FWHM) instrumental energy resolution $\Delta E_{FWHM} < 2.5\,\text{eV}$ in the soft x-ray energy range (0.3–10 keV).

A TES consists of a thin superconducting film, typically with a transition temperature $T_C \sim 0.1\,\text{K}$, weakly thermally coupled to a lower temperature heat bath via a thermal conductance G_b. The TES is self-heated to within the superconducting-to-normal phase-transition by Joule power supplied by a voltage-bias circuit, where it self-regulates on an operating point by means of electro-thermal feedback.[1] A temperature rise due to photon or particle absorption causes a subsequent change in the resistance and therefore the current flowing through the TES. This signal is read out using inductively coupled superconducting quantum interference devices (SQUIDs).

Although great strides have been made in TES detector development over the past decade, a complete physical model that describes the superconducting-to-normal transition has remained elusive. The resistive transition of a TES is conventionally considered a function of both the current I and temperature T, $R(T,I)$ and is parameterized by two important parameters: $\alpha = T/R\ \partial R/\partial T$ and $\beta = I/R\ \partial R/\partial I$. These parameters are experimentally evaluated at the quiescent operating point in the transition and are used to predict the detector signal, noise, and energy resolution.[1] This phenomenological approach does not depend on knowledge of the underlying physics that describes the superconducting-to-normal transition, but without a physical foundation, the value of this empirical description rapidly diminishes as conditions depart from the quiescent point. Recent measurements of the dependence of the critical current on the temperature, field, and size of Mo/Au proximity-bilayer structures have given new insight into the fundamental physics that describes these devices[14–16] and have highlighted the importance of the local magnetic

field environment. These results showed that the properties of these particular TESs depend on weak-link physics and long-range proximity effects. Merging this physical description with the established framework for describing TES performance could open new avenues for optimization at both the device and the instrument level. In this contribution, we present detailed measurements of critical current and $R(T,I,B)$ of a TES designed for x-ray astronomy applications and present a device model that qualitatively reproduces the observed behavior.

The paper is organized as follows. Section II presents a summary of the basic theory and equations describing TES behavior that are referenced throughout this report. Included is the background theory used to describe TESs in the context of weak links. In Sec. III, we present details of sample preparation and experimental set-up. Section IV presents measurements and discussion of the critical current as a function of magnetic field and temperature, which are compared with the basic theory developed in Sec. II. In Sec. V, we develop a simple resistively-shunted-junction (RSJ) model that is used to provide a basis for predicting $R(T,I,B)$ from the measured critical current and for the first time incorporates the role of magnetic fields on the transition characteristics. In Sec. VI, we present measurements of the parameters α and β as a function of magnetic field and bias point and compare with the predictions of the RSJ model. Also in Sec. VI, we investigate the impact of applied field on the detector responsivity and noise and compare results with the predictions based on the measured small signal detector parameters.

II. BACKGROUND THEORY

A. Basic TES principles

The TES bias circuit is depicted in Fig. 1. The TES is voltage biased using a shunt resistor (R_S) in parallel with the TES ($R(T,I)$) with $R_S \ll R(T,I)$. The TES is inductively coupled to a SQUID via an input coil with inductance of L_{in}.

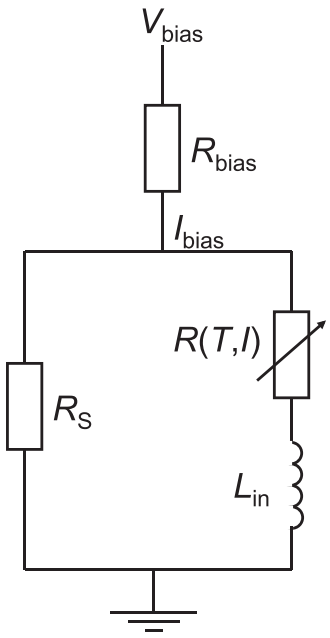

FIG. 1. TES bias circuit schematic. Since R_{bias} is much larger than the parallel combination of R_S and R(T,I), I_{bias} is essentially independent of R(T,I) and the parallel circuit is current biased.

The small signal parameters α and β, which characterize the resistive transition, determine the measured detector response to an x-ray photon of energy E. In the limit of $R(T,I) \gg R_s$ and $L_{in} = 0$, the small signal current pulse as a function of time, t is[1]

$$\Delta I(t) \approx \frac{\alpha}{1+\beta}\frac{I_0 R_0}{T_0}\frac{E}{C} e^{-\frac{t}{\tau_{etf}}}, \tag{1}$$

where R_0, I_0, T_0 are the TES resistance, current, and temperature, respectively, at the quiescent operating point and C is the device heat capacity. τ_{etf} is the electro-thermal decay time defined as

$$\tau_{etf} = \frac{\tau}{1+\mathcal{L}_0}. \tag{2}$$

Here, $\tau = C/G_b$ is the natural thermal response time of the detector, and the loop gain is defined as

$$\mathcal{L}_0 = \frac{\alpha}{1+\beta}\frac{I_0^2 R_0}{T_0 G_b}, \tag{3}$$

which parameterizes the effect of electro-thermal feedback. Both the pulse height and decay time depend on the factor $\alpha/(1+\beta)$. Whereas increasing α increases ΔI and reduces τ_{etf}, an increase in β has the opposite effect.

In an ideal TES microcalorimeter, two intrinsic sources of noise dominate. At low frequencies, the noise is dominated by thermal fluctuations between the TES and the heat sink. This noise can be considered as a white thermal noise source in series with the TES with power spectral density

$$P_n = (4k_b T_0^2 G_b F)^{1/2}. \tag{4}$$

The unit-less parameter $F(T_0,T_b,n) \sim 0.5$ accounts for the temperature gradient across the thermal link and n is a constant that depends upon the physical nature of the thermal link to the heat sink at temperature T_b.[1] At higher frequencies, the electrical Johnson noise of the TES dominates. Irwin *et al.*[17] showed that since a TES is not operated in equilibrium, an additional near-equilibrium, non-linear correction to the conventional Johnson noise should be included. The total white voltage noise in series with the TES can be described by

$$V_n = \sqrt{4k_b T_0 R_0 (1+2\beta+\vartheta^2)(1+M^2)}, \tag{5}$$

in units of $V/\sqrt{Hz}$, where the first term ($4k_b T_0 R_0$) is the linear equilibrium Johnson noise (k_b is Boltzmann's constant); the factor 2β is the first order, non-linear correction term to the noise and ϑ^2 are higher order terms in the expansion. The higher order terms include dissipationally undeterminable parameters preventing a complete solution that depends only upon known detector parameters.[17] Additional noise above the first order correction term has often been observed. This noise has the same spectral form as the Johnson noise and is

conventionally represented by the factor M^2. It has not been possible to distinguish M^2 from ϑ^2 empirically. The use of normal metal stripes perpendicular to the current flow has been shown to reduce unexplained voltage noise,[18] though the mechanism for this is not understood. In our Mo/Au devices, the first correction term in Eq. (5) has been found to account for a significant fraction of previously unexplained noise.[19] The theoretically achievable FWHM energy resolution ΔE_{FWHM} can be calculated from the noise-equivalent-power (NEP).[1] This relationship is conventionally expressed in the frequency domain as

$$\Delta E_{FWHM} = 2.355\left(\int_0^\infty \frac{4}{NEP(f)^2}\right)^{-0.5}, \tag{6}$$

where $NEP(f)^2 = \langle |N(f)|^2 \rangle / |S(f)|^2$ is the ratio of the average noise power spectral density $\langle |N(f)|^2 \rangle$, to the square of the normalized detector responsivity $S(f)$ (defined as the normalized response of the detector to an input of energy). In the small-signal limit, analytically evaluating Eq. (6) considering just the thermal-fluctuation and Johnson noise, with $R_S \ll R_0$ (strong voltage bias) and strong electro-thermal feedback, yields[1]

$$\Delta E_{FWHM} \approx 2.355\sqrt{4k_b T_0^2 \frac{C}{\alpha}\sqrt{nF(1+2\beta+\vartheta^2)(1+M^2)}}. \tag{7}$$

Thus, ΔE_{FWHM} depends on α and β explicitly as well as through any additional dependence that M^2 and ϑ^2 may have on both. Although TES microcalorimeters have already achieved impressive ΔE_{FWHM}, understanding the physical origins of α, β, M^2, and ϑ^2 is essential for further optimization.

B. TES proximity induced weak-links

There are two extreme temperature régimes in which $I_C(T,B)$ takes very different forms. We define these as a weak-link régime and strongly coupled régime. The general behavior of these régimes and the effect of self-induced magnetic fields are discussed below.

Measurements of the temperature and field dependence of the critical current of square TES bilayers[14,15] have found Josephson-junction-like behavior consistent with the devices acting as proximity-induced weak-links.[20,21] These results were described through a Ginzburg-Landau (GL) model where the TES is considered a SN′S proximity induced weak-link. The S materials are the electrical bias leads with transition temperature T_{CL} and N′ is the Mo/Au TES (see Fig. 2(a)) with intrinsic transition temperature T_{Ci} ($T_{CL} \gg T_{Ci}$). In this framework, the superconducting bias leads proximitize the bilayer material over a distance characterized by the coherence length ξ, resulting in a spatially varying superconducting order parameter, $|\psi|^2$ (see Fig. 2(b)). Through this proximity effect, the N′ material has a superconducting transition temperature that is elevated above the intrinsic Mo/Au bilayer transition temperature T_{Ci} due to the presence of the S material. Under this formalism, the critical current as a function of temperature $I_C(T)$ was

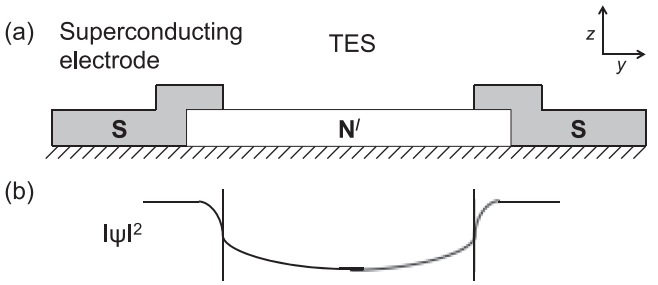

FIG. 2. (a) Schematic of SN′S proximity induced TES weak-link. The S material is the electrical bias leads with intrinsic transition temperature T_{CL} and N′ is the Mo/Au TES with intrinsic transition temperature T_{Ci} ($T_{CL} \gg T_{Ci}$). (b) Spatial variation of the modulus squared of the order parameter $|\psi|^2$ across the TES weak link.

calculated for all $T < T_{CL}$.[14,15] For $T \gg T_{Ci}$ this was described by the simplified functional form

$$IC(T,L) \propto \frac{L}{\xi(T)} e^{-\frac{L}{\xi(T)}}, \tag{8}$$

where $\xi(T) = \xi_0/|(T/T_{Ci}) - 1|^{1/2}$ is the temperature dependent GL coherence length with ξ_0 the zero temperature coherence length and L is the length of the TES. The important result from the proximity effect is that the TES is a non-uniform superconductor and even for $L \gg \xi$ and $T > T_{Ci}$ the superconducting order parameter remains finite at the center of the TES for all $T < T_{CL}$.[14,22] The GL model was also able to explain the observed scaling of T_C with L^{-2}. Later work by Kozorezov[22] described a microscopic model of a TES proximity-induced weak-link using an Usadel formalism. This model was used to calculate the spatially varying order parameter along the length of the TES, including the effect of the electron transmissivities at the SN′S interfaces, from which the critical current could be numerically calculated.

Further experimental evidence of weak-link behavior was found from the measured dependence of the critical current on magnetic field applied perpendicular to the direction of current flow, $I_C(B)$.[14–16] For $T \gg T_{Ci}$, $I_C(B)$ took a form similar to the well known Fraunhofer pattern characteristic of many Josephson structures in the limit of negligible screening (where the effective magnetic penetration[20] $\lambda_{\mathrm{eff}} \gg w$):[23]

$$I_C(B) = I_C(0)\left|\frac{\sin\left(\pi\frac{B}{B_0}\right)}{\pi\frac{B}{B_0}}\right|. \tag{9}$$

The periodicity of the oscillations is $B_0 = \Phi_0/(wL)$, where L is the junction length, w the width, $\Phi_0 = 2.07 \times 10^{-15}$ is the flux quantum. This relationship assumes a sinusoidal current-phase relationship, which corresponds to a uniform current density distribution $J(x)$ at zero applied field, and the presence of negligible screening currents. Measurements at $T \gg T_{Ci}$ on our TES test bilayers reveal critical-current patterns very similar to that predicted by Eq. (9). In those devices, L^2 was consistent with the total area of the TES contributing to the weak link. An exponential temperature dependence and Fraunhofer-like field

dependence of the critical current are a common characteristic of other superconducting-normal-superconducting (SNS) weak-link structures, such as the proximity effect micro-bridges of Ref. 24, ion-implanted micro-bridges of Ref. 25, and SNS sandwiches of Ref. 26. These results are discussed in detail in the review article of Ref. 20.

$I_C(B)$ can be related to the modulus of the inverse Fourier transform of the current distribution, thus knowledge of $J(x)$ can be used to predict $I_C(B)$ for simple geometries. Barone and Paterno use a "one-parameter" model to calculate $I_C(B)$ for cases of non-uniform tunneling-current-density distribution $J(x)$ across the width of a junction that is given by[23]

$$I_C(B) = I_C(0)\frac{\chi^2}{\chi^2\left(\pi\frac{B}{B_0}\right)^2}\left|\frac{\pi\frac{B}{B_0}\sin\left(\pi\frac{B}{B_0}\right)}{\chi\tanh(\chi)}+\cos\left(\pi\frac{B}{B_0}\right)\right|, \tag{10}$$

where $\chi = aw/2$, w is the lateral dimension across the junction, $a = J(\pm w/2)/J(0)$ is the ratio of the current density at the edges of the junction ($x = \pm w/2$) to that at the center ($x = 0$) and

$$J(x) = J_0\frac{\cosh ax}{\cosh aw/2}. \tag{11}$$

In the limit of $a \to 0$, Eq. (10) reduces to Eq. (9) for uniform $J(x)$.

Although Eq. (9) is valid for $T \gg T_{Ci}$, closer to the intrinsic bilayer temperature (but still above it), significant departures were observable. In this régime, magnetic fields generated from the transport current in the bias leads, and potentially from the current distribution from within the sample itself, can result in significant deviations from the simple model. For the square Mo/Au bilayers reported in Ref. 15, the measured $I_C(B)$ was shown to be shifted by an amount proportional to the size of the critical current, $\Delta B = g_I I_C$, where g_I is defined as the self-field factor and depends upon the geometric coupling between the TES and the bias leads. Over a broad range of TES sizes, ΔB was found to be consistent with the expected g_I calculated assuming a uniform externally applied field from the electrical bias leads.

Figure 3(a) shows a simple example of a calculated $I_C(B)$ with and without a self-induced magnetic field. The role of self-induced magnetic fields in Josephson structures is highly dependent upon the geometry. Examples for different junction geometries are discussed in Barone and Paterno and references within.[28]

As temperature is further reduced to $T < T_{Ci}$ evidence of the Josephson effect disappears and the measured critical current transitions to behavior analogous to the Meissner state for a strongly coupled superconductor[20,23] where externally applied fields are screened ($\lambda_{eff} < w$). In this régime, assuming no self-induced magnetic field and a device with symmetric edges, the $I_C(B)$ is characterized by

$$I_C(B) = I_C(0)\left(1-\frac{|B|}{B_s}\right), \tag{12}$$

where B_s is the critical field. For $|B| < B_s$ external fields are screened (Meissner region), whereas for $B > |B_s|$, it has been observed for some of our square test bilayers TESs that Josephson vortices can penetrate the film resulting in a field modulated I_C.[15] The maximum in $I_C(B)$ is shifted by the presence of self-induced magnetic fields in the same way as described above (see Fig. 3(b)).

These effects have been well characterized for featureless square TES structures, but devices used for photon and particle detection usually have additional metal features, such as metallic absorbers and noise mitigation stripes.[18,27] These additional features introduce a higher level of complexity that is not included in the one-dimensional weak-link theory described above. For the Mo/Au bilayers reported in Ref. 16, these metal features have been shown to introduce effects of non-equilibrium superconductivity and to laterally proximitize the surrounding bilayer material, which suppresses the measured T_C below that of devices without such

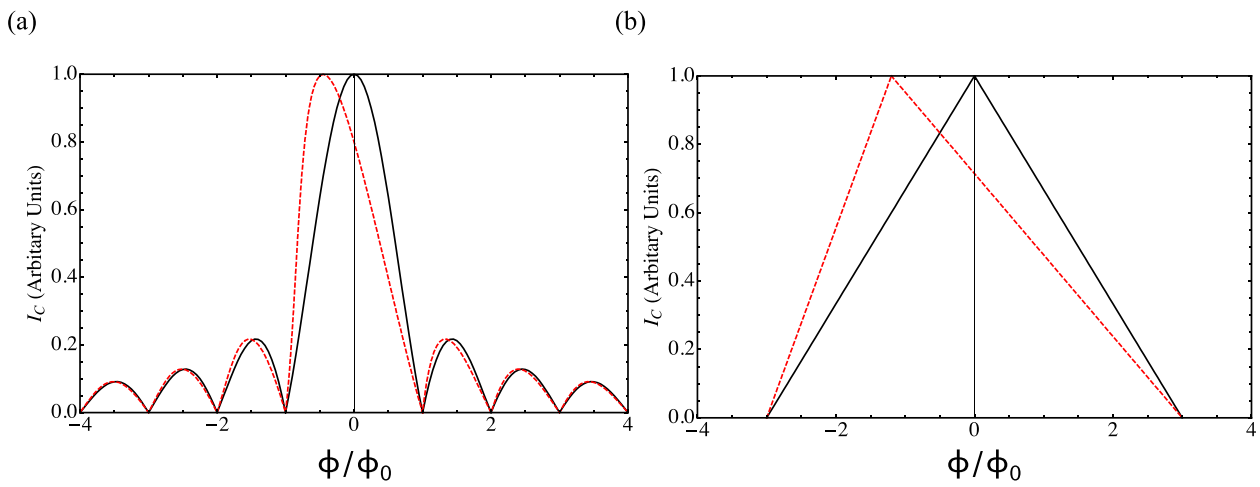

FIG. 3. (a) Example I_C as a function of applied magnetic flux Φ/Φ_0 for a narrow Josephson junction or TES weak-link in the limit $T \gg T_{Ci}$ (Eq. (9)). (b) $I_C(B)$ calculated for a wide Josephson junction or TES in the limit $T \ll T_{Ci}$ (Eq. (12)). Both figures show an example with (dashed red line) and without (solid black line) a self-induced magnetic field proportional to I_C.

features. The level of T_C shift depends on L as well as the geometry of the Au features. The role of these features on $I_C(T,B)$ has not been fully explored but might be expected to introduce a highly non-uniform current density distribution and significant deviation from the simple models described above.

III. SAMPLE DESCRIPTION AND EXPERIMENTAL SET-UP

Our TES development has focused on the use of electron-beam deposited Mo/Au proximity bilayers in which the intrinsic transition temperature of the Mo (~0.9 K) is suppressed by the proximity of the normal metal Au layer. By adjusting the thickness of the Au layer, the transition temperature can be tuned to ~100 mK. The Nb bias leads are sputter deposited. In addition, these devices utilize sputtered Au (350 nm thick) fingers that run perpendicular to the current flow and are found empirically to reduce voltage noise in the TES that has not yet been understood.[18,28] The TESs are fabricated on thin (0.5 μm) Si-N membranes, which weakly thermally couple the TES to the ~50 mK heat sink. A 4.1 μm thick overhanging electroplated Au absorber with lateral dimensions of 244 μm × 244 μm provides 96% quantum efficiency for 6 keV x-rays. These absorbers make contact with the TES and surrounding membrane area in a "T"-shaped region. This "T"-shaped absorber attachment stem is 15 μm wide and strongly thermally couples the absorber to the sensor. The TES geometry is shown in Fig. 4. The detectors are voltage biased using a shunt resistor of $R_S = 0.2\,\text{m}\Omega$. The Mo/Au has a normal resistance of 16 mΩ per square. The presence of the addition Au features shown in Fig. 4 provides parallel paths that reduce the normal state resistance of the device to $R_n \approx 8\,\text{m}\Omega$. The device tested here is from a wafer from the same fabrication run as those described in Refs. 27 and 29. Further details of these devices may be found in those references.

These experiments were carried out in an adiabatic demagnetization refrigerator (ADR) with an operational base temperature of 50 mK. A 400-turn superconducting field coil approximately 3 mm above the detector chip was used to vary the magnetic field perpendicular to the plane of the TES film. The field coil was calibrated at 4.2 K using a SQUID magnetometer provided by Physikalisch-Technische Bundesanstalt (PTB) Berlin. The applied field is calculated to vary by <0.1% over the length scale of the TES and a few % over the 2 mm length scale of a 8 × 8 pixel array. The detectors were housed within a superconducting Nb box to shield against external magnetic fields. This box trapped in a residual magnetic field of $< 1\,\mu$T, which varied day-to-day over the course of an experimental run. Any stray field will suppress the measured transition temperature, thus by measuring the applied field required to maximize the transition temperature we can track the environmental field to ~0.05 μT. For ease of comparison, all data throughout this report are presented with the required nulling field subtracted from the applied magnetic field.

IV. CRITICAL CURRENT MEASUREMENTS AND ANALYSIS

The critical current at different applied magnetic fields and temperatures is derived from measurement of the TES current I as a function of the voltage V applied to the electrical bias circuit shown in Fig. 1. The voltage is swept symmetrically around zero at a rate of typically 0.2–0.6 Hz, which was required to avoid thermal hysteresis from normal-state self-heating that can suppress the measured I_C. The resulting data are digitized. The field is then incremented before repeating the measurement. For a particular field, I_C is determined from the first on-set of resistance for both the positive I_{C+} and negative I_{C-} bias direction. The data are sampled every ~0.02 μT over a range of several μT. The ADR temperature is controlled during acquisition to ensure temperature stability.

Figure 5 shows the measured $I_{C+}(B)$ for the positive bias direction at $T = 84.4$ mK. The transition temperature of the device (measured at an excitation current of ~100 nA) is 85.1 mK at zero applied magnetic field. These data are compared with a simple Fraunhofer diffraction pattern of Eq. (9) and the one-parameter model of Eq. (10). The data show modulation of the I_C with applied magnetic field that is indicative of weak-link behavior in this device. However, two

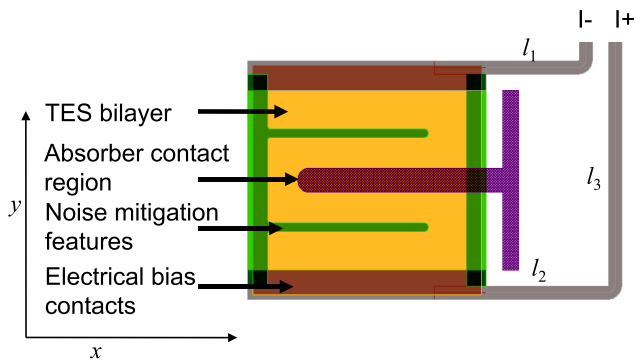

FIG. 4. Schematic diagram of 140 μm × 140 μm Mo(45 nm)/Au(190 nm) TES. The absorber attachment stem is in a "T" configuration. The bias current flows in the vertical direction. The three components that make up the electric bias leads are labeled l_1, l_2, and l_3.

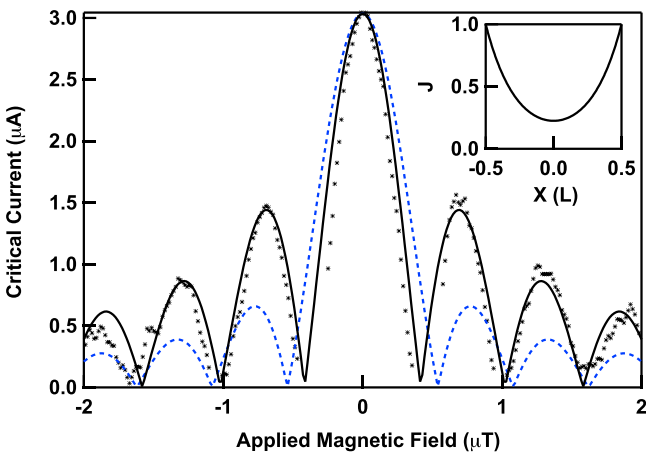

FIG. 5. Measured $I_C(B)$ for a Mo/Au TES as depicted in Fig. 4. The data are fitted using Eq. (10) with a = 4.4 (solid black line). Also shown for comparison is the Fraunhofer pattern of Eq. (9) assuming uniform J(x) (blue dashed line). The inset shows the corresponding J(x) calculated from Eq. (11).

significant deviations from the behavior seen in plain devices are observed. Firstly, whereas the square devices were well represented by Eq. (9) for uniform $J(x)$, the data for this device are better approximated by the one-parameter model (Eq. (10)) with a fit value of $a = 4.4$. This is characterized by a narrower central maximum region and larger secondary maxima to either side of the central maximum compared with that predicted from Eq. (9). For a simple junction geometry, this would suggest non-uniform Josephson coupling with $J(x)$ significantly peaked at the edges (as shown in the inset). However, whether this is the correct physical interpretation for these complex three dimensional geometries with lateral features perpendicular to the current injection is not proven. The second difference is that the periodicity of the oscillations is $B = 0.55 \pm 0.02\,\mu$T, corresponding to an area $wL \approx 3600\,\mu\text{m}^2$ contributing to the weak-link. For a square geometry this would imply a lateral dimension of 60 μm. Thus, the size of the contributing weak link is ~20% the area of the total $140 \times 140\,\mu$m Mo/Au bilayer or ~34% of the bilayer area not covered by additional deposition layers. For comparison, the featureless devices reported in Ref. 15 had a weak-link area equal to the total bilayer area L^2 (in the range $L = 8$–$240\,\mu$m).

In Figs. 6 and 7, we show $I_{C+}(B)$ and $I_{C-}(B)$ over the temperature range 84.4–41.7 mK. The data are reproducible, non-hysteretic, and exhibit time-reversal symmetry ($I_{C+}(B) = -I_{C-}(-B)$), suggesting that the film is free of trapped flux, which may occur at impurity sites or the SNS interfaces. Four different devices of the geometry shown in Fig. 4 were tested, and all revealed similar temperature and field dependence, confirming the results are a characteristic of this particular device geometry. As the temperature is lowered, $I_C(B)$ deviates rapidly from the weakly coupled behavior described above. Though oscillatory behavior is still apparent, the minima in the $I_C(B)$ do not go to zero and the maximum in $I_C(B)$ show a clear shift away from zero applied field, which is increasing with decreasing temperature (see Fig. 6). As the temperature is reduced below 83 mK, the oscillations to the right of the maximum (for $I_{C+}(B)$) grow significantly and in the range 70–76 mK the oscillations are of similar magnitude. The periodicities of the oscillations over this temperature range are approximately the same as seen for the weakly coupled régime for $T \approx 84$ mK. As the temperature is lowered further, the field required to maximize $I_C(B)$ begins to shift to the opposite direction. Below 70 mK (Fig. 7(b)), the data have linear-like regions similar to the ideal Meissner screening state described by Eq. (12). However, even at the lowest temperatures measured, there is still oscillatory behavior superimposed on the linear-like regions, suggesting that weak-link physics effect are still involved (Fig. 8 shows an expanded view of the data in Fig. 7(b), illustrating the oscillatory behavior at $T = 70.4$ and 53 mK).

In the simple self-field model outlined in Sec. II B, which assumes an externally applied magnetic field from the biasing leads, a shift ΔB in the field at which the maximum $I_C(B)$ occurs is expected. The magnitude of the shift, ΔB, should be proportional to the magnitude of I_C. However, the results show some departures from this behavior. Figure 9(a) shows the maximum $|I_C(B)|$ for each measured temperature versus the applied field required to maximize both $I_{C+}(B)$ and $|I_{C-}(B)|$. In Fig. 9(b), the same magnetic field values are presented as a function of the temperature. To aid comparison between common data points shown in Figs. 6–8 and Fig. 9, five data points corresponding the maximum $I_C(B)$ for different temperatures are labeled *A*-*E*. Although the maximum $|I_C(B)| < \sim 100\,\mu$A appears to track approximately linearly with current at a rate of $g_I \approx -16\,\mu$T/mA, it also appears linear with temperature at a rate of $g_T \approx 0.28\,\mu$T/mK. The estimated magnitude of the self-induced magnetic field at the center of the device from the three components that make up the electrical bias leads (labeled l_1, l_2, l_3 in Fig. 4) is calculated to be $g_I \approx 5\,\mu$T/mA. This is smaller in magnitude and, most surprisingly, of the opposite polarity to the measured shift. Further discrepancy can be found in the shape of $I_C(B)$. Shown in Fig. 10 is the measured $I_C(B)$ for $T = 83.5$ mK,

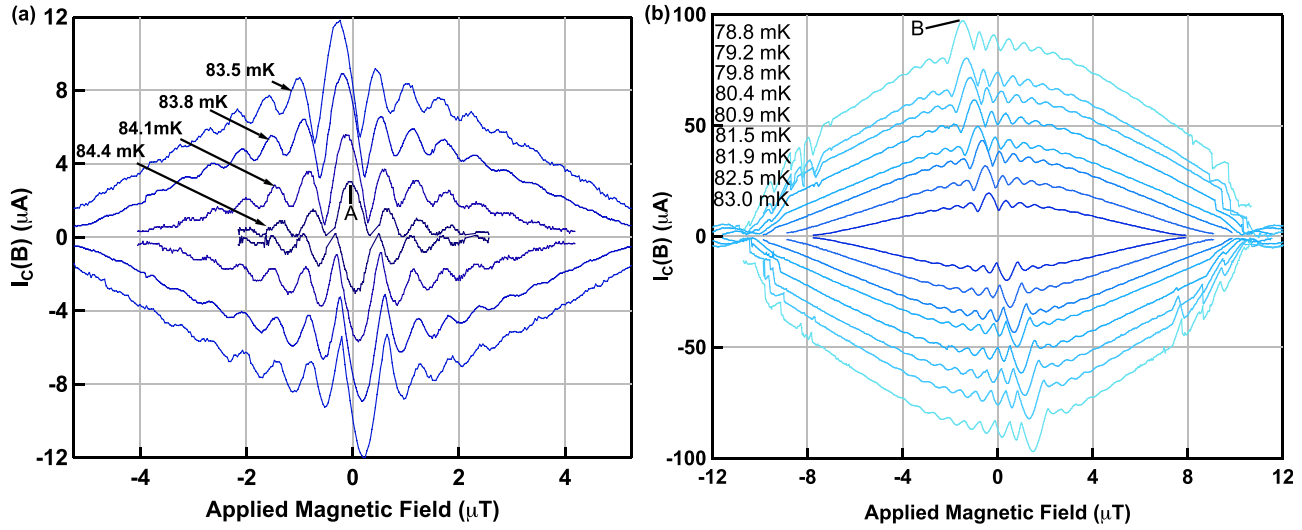

FIG. 6. (a) Measured $I_{C+}(B)$ and $I_{C-}(B)$ for the temperature range (a) 84.4–83.5 mK and (b) 78.8–83.0 mK. The temperature corresponding to each trace is indicated on the figure. Because of the high density of sampling (~0.02 μT), the data appear as continuous lines. The statistical error in I_C is estimated to be $\pm 0.05\,\mu$A. For reference with Fig. 9, the maximum I_C for T = 84.4 mK and T = 78.8 mK are labeled A and B, respectively.

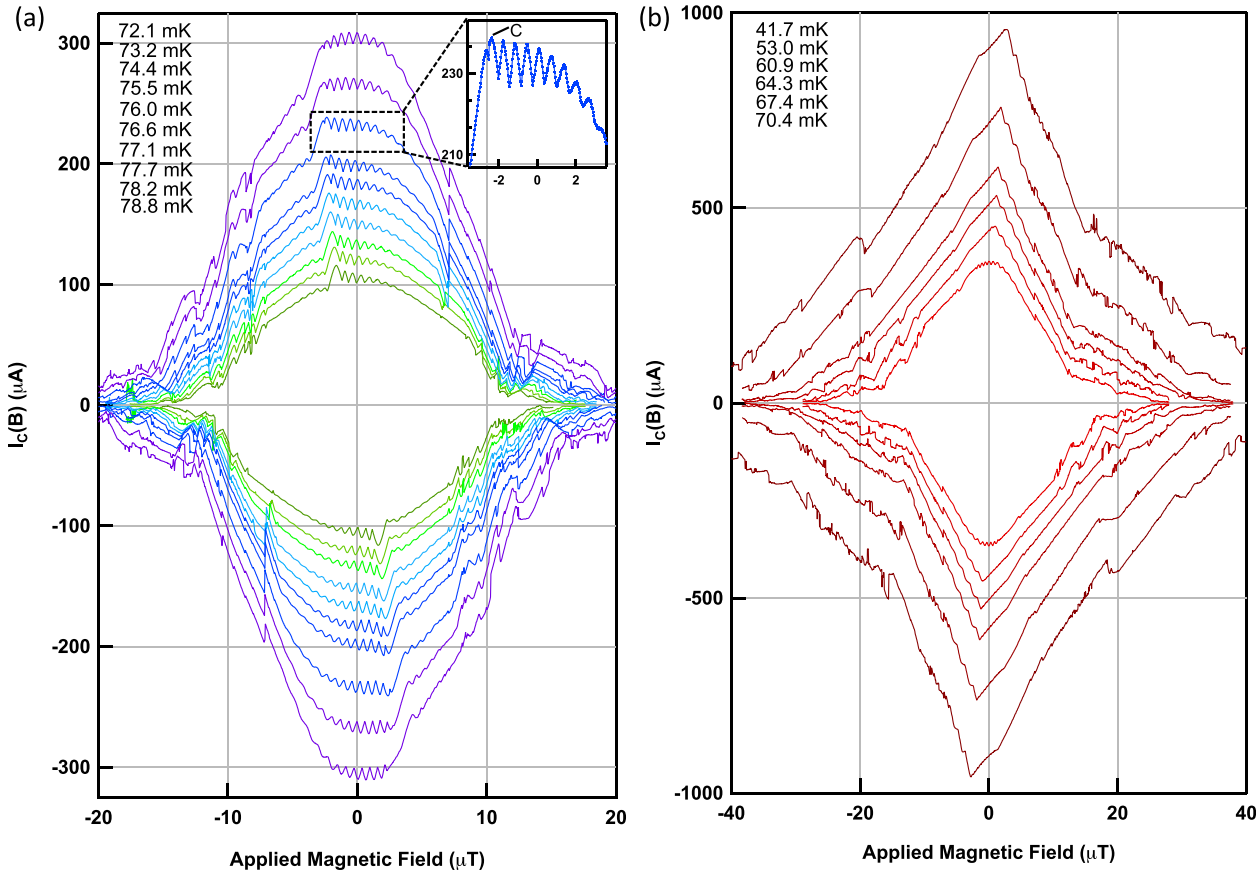

FIG. 7. Measured $I_{C+}(B)$ and $I_{C-}(B)$ for the temperature range (a) 72.1–78.8 mK and (b) 70.4–41.7 mK. The temperature corresponding to each trace is indicated on the figure. Because of the high density of sampling ($\sim 0.02\,\mu$T), the data are plotted as continuous lines. The inset in (a) shows a zoom-in of the data corresponding to 74.4 mK. The maximum value of I_C is labeled C for reference with Figure 9.

presented is just the region of the central peak. Shown for comparison are two Gaussians with the same width as the central peak. A shift is introduced such that the peak in the Gaussian matches the peak in the data, however, one is shifted an amount proportional to temperature ($\Delta B = g_T(T - T_{C0})$ where $g_T = 0.3\,\mu$T/mK and the constant $T_{C0} = 84.5$ mK is the fitted transition temperature in the limit $I_C = 0$) and the other proportional to the critical current ($\Delta B = g_I I_C$, where $g_I = -20\,\mu$T/mA). This comparison suggests that the data are better described by a shift proportional to T as opposed to proportional to I_C as predicted by a self-field from the electrical bias leads.

In the Meissner-like region ($T < 70$ mK), the field and temperature evolution of the I_C is more consistent with a simple self-field model where the shift is proportional to current. In this régime, we find $g_I \approx 3\,\mu$T/mA, within a factor of two of the estimated self-field factor from the bias leads.

Though a detailed theory to quantitatively describe these results for such complex geometries is absent, the measurements are qualitatively similar to the theory outlined in Sec. II for simple geometries, illustrating a weak-link régime transitioning to a Meissner-like state. We believe the differences can be attributed to the additional metal features introducing a non-uniform current density with a complex temperature and magnetic field evolution. In addition to the self-induced field from the electrical bias leads, the current in the TES itself may be generating a significant contribution. Since the coherence length and penetration depth both

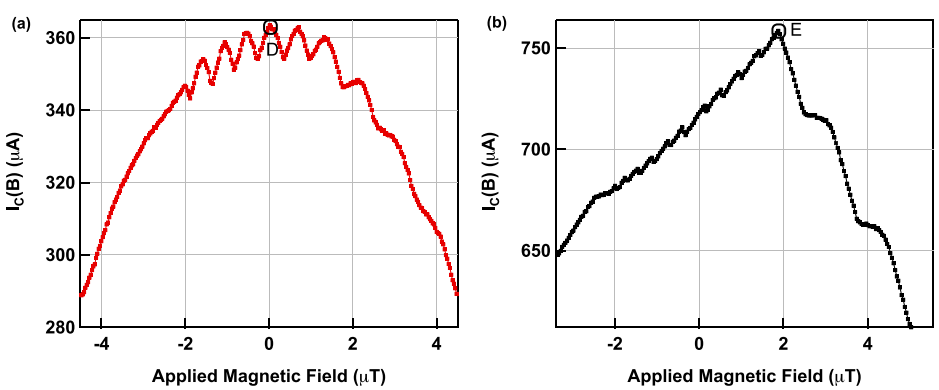

FIG. 8. Measured $I_{C+}(B)$ for (a) 70.4 mK and (b) 53.0 mK. The plots are expanded views of curves shown in Fig. 7(b) to illustrate the fine oscillatory structure in $I_C(B)$ at lower temperatures. The maximum values of I_C are labeled D and E for reference with Figure 9.

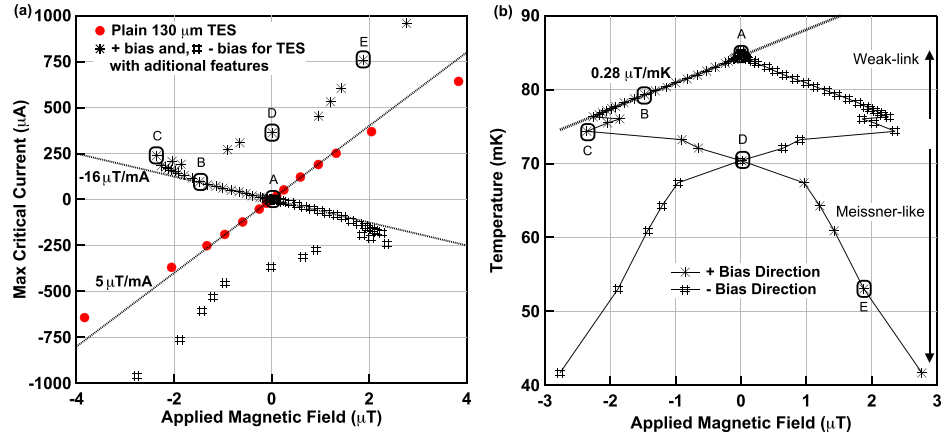

FIG. 9. (a) Maximum of $I_C(B)$ as a function of applied magnetic field for measurements made in the range 85.3–41 mK (* symbols). Data for both I_{C+} (* symbols) and I_{C-} (# symbols) are shown. The approximately linear region (corresponding to $g_I \approx -16\,\mu T/mA$) for $T > 80$ mK is indicated by a dotted line. Shown for comparison is data for a 130 μm plain square device with no additional metal features (circle symbols) but similar bias lead geometry.[19] Here, the data agree well with the calculated self-field factor shown by the second dotted line (corresponding to $g_I \approx 5\,\mu T/mA$). (b) The field at which the maxima in $I_C(B)$ occurs as a function of temperature. The dotted line shows the region ($T > 76$ mK) where the $I_C(B)$ shifts approximately linearly with temperature at a rate $g_T \approx 0.28\,\mu T/mK$. To aid comparison between the common data points shown in this figure, the same five data points are circled in both (a) and (b) for the positive bias direction only. These are labeled A-E in both figures and correspond to the same labeled data points in Figs. 6–8.

get smaller with decreasing temperature, the current distribution (and therefore any internally generated self-induced field) is likely to also be a complex function of temperature. We are in the process of designing and fabricating devices with different TES and bias lead geometries to further investigate the role of self-induced magnetic field on the $I_C(T,B)$.

V. MODELING THE RESISTIVE TRANSITION OF A TES

A. Basic equations

The observed weak-link behavior in these TESs opens up opportunities to develop a model for the resistive transition. Kozorezov *et al.*[30] recently proposed the well-known RSJ model for a TES with no additional metallic features. The RSJ model has been successfully used to describe the properties of many different Josephson Junctions and also weak-links.[20,23,31,32] In the RSJ model, the junction is represented as a two-element circuit model. An Ohmic resistor represents the quasiparticle current branch and a Josephson junction the super-current branch. Irwin[33] proposed a similar two fluid model of a TES. In that model, the proposed resistance mechanism originates from quasi-particle recombination across phase-slip lines as described by Skocpol-Beasely-Tinkham.[34] This model has recently been revisited and compared with data,[35,36] though the potential role of self-induced magnetic field modulation of the critical current has not been considered for this or the RSJ model. Given the weak-link behavior observed over a broad temperature range in our devices, we use the RSJ approach as a starting point. This simple one-dimensional model is derived assuming a sinusoidal current-phase relation and uniform current density distribution, assumptions that are unlikely to be true given the complex geometry of the TES and how the measured $I_C(B)$ deviates from the classical Fraunhofer pattern even for $T \gg T_{Ci}$. Furthermore, the RSJ model does not include non-equilibrium superconductivity effects, such as charge imbalance and Andreev reflection, which may also play a significant role in determining the transition characteristics. Ambegaokar and Halperin[37] investigated the role of thermal fluctuation effects on the RSJ model for different limiting cases. More recently, Coffey[31] presented a complete analytical solution, incorporating these limiting cases, which was suggested by Kozorezov[30] as a possible model for the TES weak-link. We use the numerically and analytically simpler Ohm's law with the correction factor of Ambegaokar and Halperin,[37] which is valid in the limit of the Josephson coupling energy much bigger than the thermal energy $\hbar I_C(T)/2e \gg k_b T$ and $I/I_C > 1$. This is a valid limit for the devices presented here and numerical simulations confirm negligible difference between the two approaches except for very low in the transition (a few % R_n), where thermally activated flux flow is predicted to broaden the transition. This is not generally a régime of interest for the device presented here since optimum performance is achieved at operating points > 10% R_n. Generalizing to include the magnetic field dependence of the critical current, the resistive transition $R(T,I,B)$ can be written as

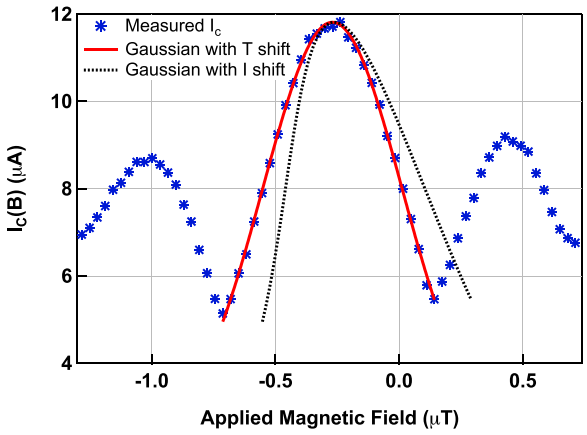

FIG. 10. Measured $I_{C+}(B)$ for $T = 83.5$ mK. The solid line shows a Gaussian of the same width as the central oscillation with an offset $\Delta B \propto (T - T_{C0})$. The dotted line was produced with $\Delta B \propto I_C$.

$$\frac{R(T,I,B)}{R_n} = \sqrt{1 - \left(\frac{I_C(T,B)}{I}\right)^2}, \tag{13}$$

which is valid for $I/I_C > 1$. In the limit $I/I_C < 1$, the device is superconducting ($R(T,I,B) = 0$) and for $I/I_C \gg 1$, it is normal ($R(T,I,B) = R_n$). It is not possible to accurately reproduce the highly complex $I_C(T,B)$ seen in the measured data in a simple functional form. Thus in the following calculations, we use a simple model of $I_C(B)$ described by Eq. (10), where $I_C(0)$ is determined from a high order polynomial fit to the measured maximum in $I_C(B)$ as a function of temperature. In order to incorporate some of the basic effects presented in the measured $I_C(T,B)$, such as a current and temperature dependent offset to B that could potentially arise due to a self-induced magnetic field, for example (either internal to the sensor or externally applied from the bias leads), we introduce a simple linear current dependent ($g_I I$) and temperature dependent ($g_T T$) offset to the oscillations in the critical current

$$\Delta B(T,I) = g_I I + g_T(T - T_{C0}), \tag{14}$$

where $T_{C0} = 84.5$ mK is the upper limit on the temperature range. In the presence of an externally applied magnetic field, B_{ex}, the total field is then described as $B = B_{ex} + \Delta B(T,I)$. The small signal transition parameters α and β, are then calculated by directly differentiating Eq. (13)

$$\begin{aligned}
\alpha(T,I,B) &= \frac{T}{R}\frac{\partial R}{\partial T} \\
&= -\frac{1}{(x_i^2 - 1)}\frac{T}{I_C(T,B(T,I))} \\
&\quad \times \left(\frac{\partial I_C(T,B(T,I))}{\partial T} + \frac{\partial B(T,I)}{\partial T}\frac{\partial I_C(T,B(T,I))}{\partial B(T,I)}\right) \\
&= -\frac{1}{(x_i^2 - 1)}\frac{T}{I_C(T,B(T,I))} \\
&\quad \times \left(\frac{\partial I_C(T,B(T,I))}{\partial T} + g_T\frac{\partial I_C(T,B(T,I))}{\partial B(T,I)}\right) \\
&= -\left(\left(\frac{R_n}{R}\right)^2 - 1\right)\frac{T}{I_C(T,B(T,I))} \\
&\quad \times \left(\frac{\partial I_C(T,B(T,I))}{\partial T} + g_T\frac{\partial I_C(T,B(T,I))}{\partial B(T,I)}\right),
\end{aligned} \tag{15}$$

where $x_i = I/I_C(T,B(T,I))$. The last line is achieved by substituting Eq. (13) for the pre-factor $(x_i^2 - 1)^{-1}$. We can similarly derive

$$\begin{aligned}
\beta(T,I,B) &= \frac{I}{R}\frac{\partial R}{\partial I} \\
&= \frac{1}{(x_i^2 - 1)}\left(1 - x_i\frac{\partial B(T,I)}{\partial I}\frac{\partial I_C(T,B(T,I))}{\partial B(T,I)}\right) \\
&= \frac{1}{(x_i^2 - 1)}\left(1 - g_I x_i\frac{\partial I_C(T,B(T,I))}{\partial B(T,I)}\right) \\
&= \left(\left(\frac{R_n}{R}\right)^2 - 1\right)\left(1 - g_I x_i\frac{\partial I_C(T,B(T,I))}{\partial B(T,I)}\right).
\end{aligned} \tag{16}$$

The last term in both Eqs. (15) and (16) arise due to the T and I dependence, respectively, of B (Eq. (14)). Different functional forms of Eq. (14) would result in different dependences seen in α and β.

B. Numerical simulations of the resistive transition

In this section, we use the basic equations for the RSJ model to calculate the $R(T,I)$ surface as a function of different externally applied fields. When biasing the TES with the electric circuit depicted in Fig. 1, it is only possible to sample a narrow contour of the $R(T,I)$ surface that is determined by the power balance between the Joule heating in the TES and the power flow to the heat bath,

$$I^2 R(T,I) = K(T^n - T_b^n), \tag{17}$$

where K is a constant with units WK^{-n}. The solution of this power balance is the path along $R(T,I)$ on which the TES is operated. In these simulations, the power balance equation is numerically solved to determine the bias path on the $R(T,I)$ surface for each applied magnetic field, from which α and β are directly calculated from the partial derivatives of $R(T,I)$. For a constant applied I_{bias} to the circuit in Fig. 1, a change in the $R(T,I)$ due to a change in field will result in a change in equilibrium operating resistance. This is constrained by the circuit equation $R(T,I) = (I_{bias}/I - 1)R_s$, which we re-calculate for each applied field. We present four different test cases with different combinations of g_I and g_T to illustrate the effect on the transition characteristics. The values of g_I and g_T are chosen to be representative of the magnitude of the shifts seen in the critical current data presented in Sec. IV.

1. Case 1: $g_I = 0$, $g_T = 0$

In our first test case, we assume no current or temperature dependence of B (Case 1: $g_I = 0$, $g_T = 0$). The calculated $I_C(B)$ functions for a series of different fixed temperatures are shown in Fig. 11(a). From this $I_C(T,B)$, we can calculate the resistive transition $R(T,I)$ for a fixed applied magnetic field using Eq. (13). The calculated $R(T,I)$ surface is shown in Fig. 11(b) for $B_{ex} = 0$. The path followed as I_{bias} is increased is shown for $T_b = 55$ mK with $K = 1.2 \times 10^{-8}$ $\mathrm{WK}^{-3.2}$ and $n = 3.2$, which were determined experimentally from measurements of TES bias power (I^2R) as a function of T_b in the range 50–85 mK (for a zero externally applied magnetic field).

Figure 12 shows α and β as a function of R/R_n along the calculated bias path. In this case $g_I = 0$ and β reduces to the simple form $(R_n/R)^2 - 1$. Thus, β is predicted to only depend upon the resistance within the transition. The functional form of α depends upon this same pre-factor as β, but also includes an additional dependence upon the derivative T/I_C $\partial I_C/\partial T$. In Fig. 12, $\alpha(R/R_n)$ is shown for two examples of applied field, $B = 0\,\mu$T and $B = 0.4\,\mu$T, which correspond to the maximum and first minimum in the $I_C(B)$, respectively. In Fig. 13(a), we show T/I_C $\partial I_C/\partial T$ as a function of temperature for three fields $B = 0$, $0.4\,\mu$T, and $0.7\,\mu$T (the latter corresponding to the second maxima in the $I_C(B)$). As the field

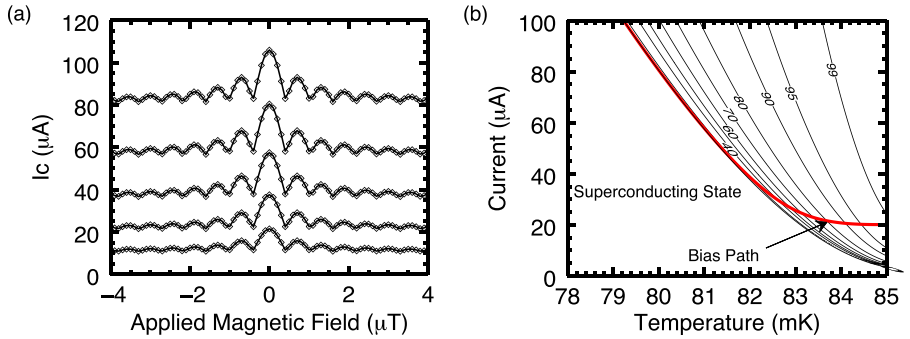

FIG. 11. (a) Calculated $I_C(B)$ for Case 1 ($g_I = 0$, $g_T = 0$) for temperatures $T_b = 79$–83 mK (in 1 mK increments in order of decreasing I_C). The circles show the modeled data calculated at 0.1 μT increments. (b) Calculated R(T,I) surface using the $I_C(T,B)$ for $B_{ex} = 0$. Plotted on the surface are contours of constant percentage R/R_n (thin black lines). Also shown is the bias path defined as the resistance where the bias power is equal to power flow to the heat bath (thick red line).

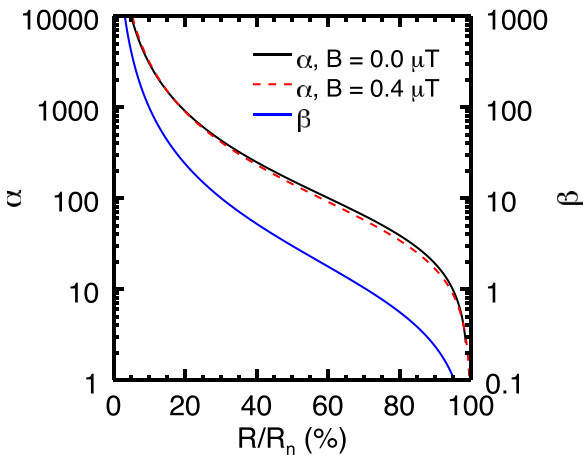

FIG. 12. Calculated $\alpha(R/R_n)$ along the bias paths for $B = 0\,\mu$T and $B = 0.4\,\mu$T (left axis). Also shown is $\beta(R/R_n)$ (right axis). The data are calculated from the modeled $I_C(T)$ for Case 1 ($g_I = 0$, $g_T = 0$). For a fixed R/R_n, β is independent of externally applied field whereas α is not.

is changed, for a fixed T, $T/I_C\ \partial I_C/\partial T$ is modulated with the same phase as $I_C(B)$ and has a maximum at $B = 0$ and a minimum at 0.4 μT. Thus, these curves bound the maximum variation in α for a fixed temperature. For constant resistance, the inset in Fig. 13(a) illustrates how the TES temperature (at 20% R_n in this example) will oscillate in phase with the $I_C(B)$ oscillations. The complete resistances versus temperature plots are provided on Fig. 13(b) for the three examples for different applied fields. Since $T/I_C\ \partial I_C/\partial T$ varies with temperature, $\alpha(B_{ex})$ for constant R can take different forms depending upon the magnitude of the field dependence of the temperature oscillations. Fig. 14(a) shows $\beta(B_{ex})$ and $R(B_{ex})/R_n$ for an example of constant $I_{bias} = 262\,\mu$A, and Fig. 14(b) shows $\alpha(B_{ex})$ for both constant R/R_n and constant I_{bias}. For the case of constant I_{bias}, the TES resistance is not constant with the applied field and will oscillate with in phase with the $I_C(B)$. In this case, the pre-factor $(R_n/R)^2 - 1$ dominates over $T/I_C\ \partial I_C/\partial T$ and $\alpha(B_{ex})$ takes the form of $\beta(B_{ex})$. In the example presented in Fig. 14(b) for fixed resistance of 20% R_n, only the derivative term is varying as temperature changes and α is only weakly dependent upon applied field, varying by ~3%. It also has a very different shape compared with the constant I_{bias} case. Note that these observations are specific to the example presented and relatively small changes in $I_C(T,B)$ can make significant changes in how these terms combine to give $\alpha(B_{ex})$. In this first test case, the $I_C(T,B)$ is identical for both positive and negative bias directions, α and β will similarly be identical for both bias directions, $\alpha_+ = \alpha_-$ and $\beta_+ = \beta_-$.

2. Case 2: $g_I \neq 0$, $g_T = 0$

In our second test case, we introduce a current dependent shift to the magnetic field. This case can arise due to a self-induced magnetic field (as discussed in Sec. IV) that is proportional to the current, $\Delta B = g_I I$ (Case 2: $g_I \neq 0$, $g_T = 0$).

Figures 15(a) and 15(b) show the calculated $I_C(B)$ and $R(T,I)$ surface, respectively, incorporating a current-dependent offset, $\Delta B = g_I I$ with $g_I = 5\,\mu$T/mA. Since the resistive transition is fundamentally a function of current, ΔB is changing throughout the resistive transition. Thus, it follows that features will appear in the $R(T,I)$ surface as the

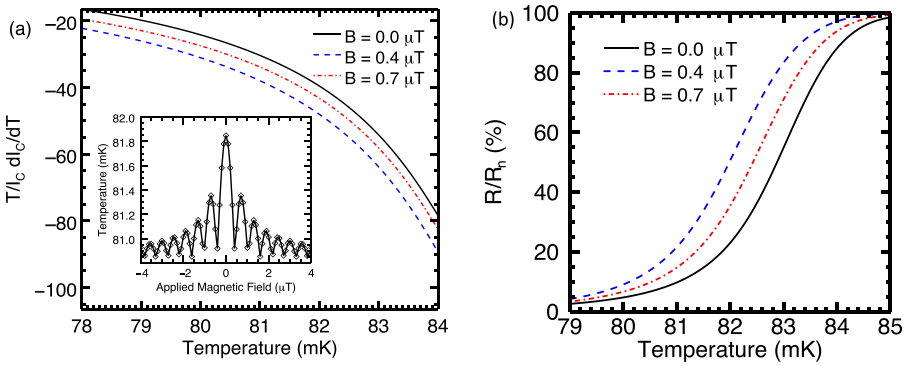

FIG. 13. (a) Presented is $T/I_C\ \partial I_C/\partial T$ as a function of temperature for $B = 0\,\mu$T, $0.4\,\mu$T, and $0.7\,\mu$T. These approximately correspond to the maximum, first minima, and second maxima in the $I_C(B)$. The inset shows the TES temperature as a function of applied field for 20% R_n. The resistance versus temperature curves for the three example fields is shown in (b).

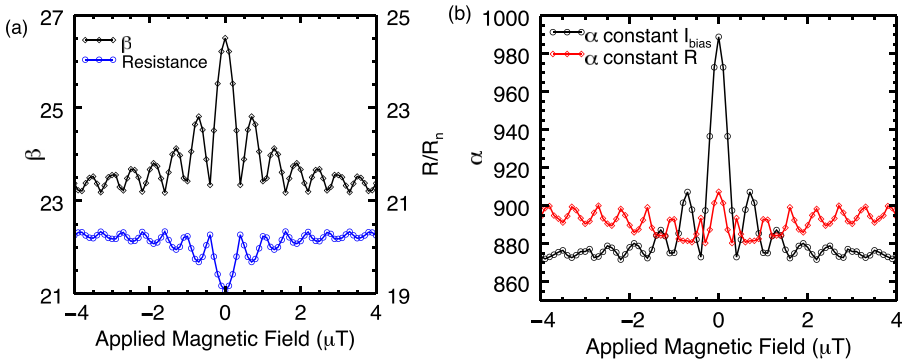

FIG. 14. Presented in (a) is the calculated $\beta(B_{ex})$ (left axis) and R/R_n (right axis) both for constant $I_{bias} = 262\,\mu A$. Also presented in (b) is $\alpha(B_{ex})$ for both constant I_{bias} and for constant $R/R_n = 20\%$. Unlike β, α varies with applied field for constant resistance.

I_C is modulated. This is highlighted in Fig. 15(b) by the dotted line, which corresponds to the position of the first minimum $\Delta B = 0.42\,\mu T$ in $I_C(B)$ (see Fig. 11(a)), this appears along a line of constant current in the $R(T,I)$ at $I = \Delta B/g_I = 84\,\mu A$. Above and below this line, there is a discrete change in the direction of the contours of constant R/R_n.

When compared with Case 1 with $g_I = 0$, we see that β has an additional dependence on the product of the magnitude of g_I and the derivative $\partial I_C/\partial B$ (Eq. (16)). Figure 16(a) shows $\beta(R/R_n)$ for a series of different fields ($B_{ex} = 0.0$, -0.1, $-0.2\,\mu T$). As the bias path intersects a minimum, a discrete change in the magnitude of the $\partial I_C/\partial B$ occurs. This results in a discrete change in the magnitude of β. In the presence of an externally applied field, the position of a minimum in $I_C(B)$ will shift position in the $R(T,I)$. This feature will occur at the position in the transition that corresponds to a current $I = (B_i - B_{ex})/g_I$, where B_i is the position of the specific feature in the $I_C(B)$. Thus, in contrast to the $g_I = 0$ case, $g_I \neq 0$ will mean that even for a fixed resistance $\beta(B_{ex})$ will vary with B_{ex}. Increasing g_I means that the phase will change more rapidly with current and more of these features will appear in the transition, and the magnitude of the discontinuities will be larger. Although the discrete changes in $\beta(R/R_n)$ at the discontinuities in the derivative term are most obvious, β will be modified at all points in the transition as the current continuously changes.

For a fixed resistance in the transition, β will vary with applied field due to the derivative term in, $\partial I_C/\partial B_{ex}$, Eq. (16). For constant resistance, neither temperature nor current is constant with applied field. However, it is interesting to compare the exact form of $\beta(B_{ex})$ with that estimated by assuming constant temperature. For constant R/R_n and constant T, the form of $\beta(B_{ex})$ can be determined from $\partial I_C/\partial B_{ex}$ in Eq. (16) from a $I_C(B)$ at constant T. Fig. 16(b) compares $\beta(B_{ex})$ calculated using the assumption of constant T (81 mK) and R (20% R_n), with the direct calculation from the partial derivative of the $R(T,I)$ surface at 20% R_n. Thus in this example, these two methods agree quite well suggesting that directly differentiating a single measured $I_C(B)$ for a fixed temperature can be a good approximation for the expected form of $\beta(B_{ex})$. Figure 17(a) shows three examples of $\beta(B_{ex})$ for different constant I_{bias}, which correspond to three different R/R_ns' For constant I_{bias}, if g_I is small, $\beta(B_{ex})$ may still be dominated by the pre-factor in Eq. (16), $(R_n/R)^2 - 1$. However if the magnitude of the self-field is sufficiently large, the oscillations $\beta(B_{ex})$ will take the form of the derivative of $I_C(B)$ and will therefore have a different shape and phase from $I_C(B)$ (as is the case in this example). Since the derivative term oscillates between positive and negative, $\beta(B_{ex})$ can be either smaller or larger than Case 1 for $g_I = 0$. Increasing g_I has the effect of increasing the peak-to-peak height of the oscillations in $\beta(B_{ex})$ but the phase will be unchanged. Both the magnitude and phase of the oscillations vary with bias point in the transition (R/R_n).

Although incorporating a current dependent term to the critical current does not explicitly change the temperature dependence of I_C, $\alpha(B_{ex})$ will be modified compared with case 1. $\alpha(B_{ex})$ will be skewed such that the maximum will occur at an applied field corresponding to $B_{ex} = -g_I I$. Thus in this case, $\alpha(B_{ex})$ oscillates with a phase similar to $I_C(B_{ex})$,

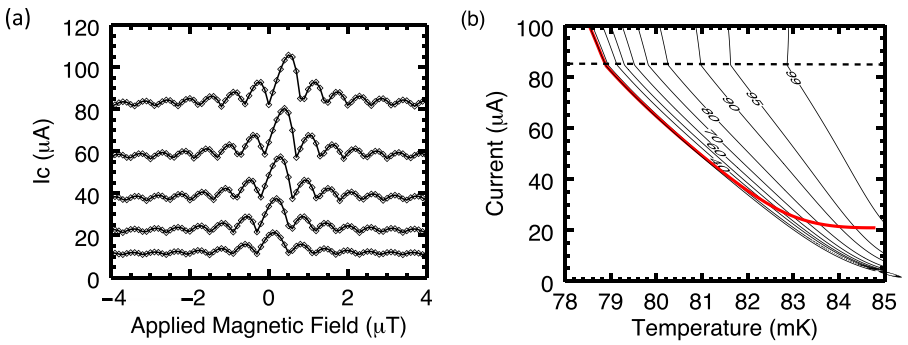

FIG. 15. (a) Calculated $I_C(B)$ for Case 2 ($g_I = 5\,\mu T/mA$, $g_T = 0$) for T_b in the range 79–83 mK (in 1 mK increments in order of decreasing I_C). (b) Calculated R(T,I) surface using the $I_C(B)$ for zero externally applied magnetic field. Plotted on the surface are contours of constant percentage R/R_n (thin black lines). Also shown is the bias path defined as the resistance where the bias power is equal to power flow to the heat bath (thick red line). The dotted line indicates the intersection with the first minimum in the $I_C(B)$ at a current of $I = \Delta B/g_I = 84\,\mu A$.

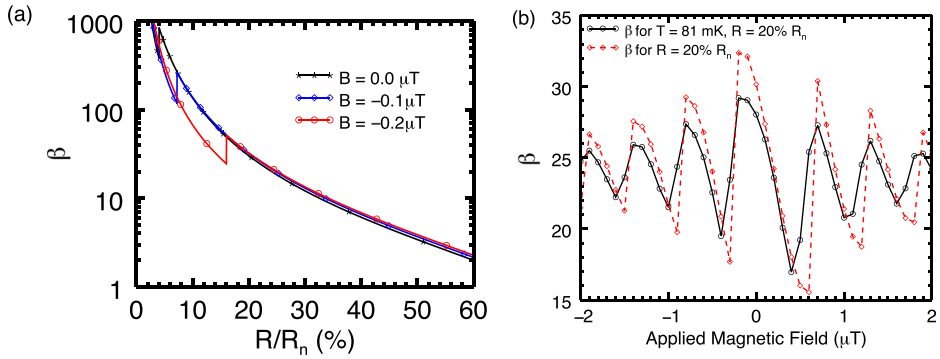

FIG. 16. (a) Presented is the calculated β as a function of R/R_n for three different applied magnetic fields (as indicated on the figure). The discontinuities in $\beta(R/R_n)$ arises from discontinuity in $\partial I_C/\partial B$ at the minima in $I_C(B)$. As the externally applied field is changed, the position of these features will move to a different part of the transition. (b) β as a function of field for two examples. Firstly (dashed-dot line), calculated directly from the partial derivative of the R(T,I) surface for constant resistance ($R = 20\%\ R_n$) and secondly (solid line) calculated from Eq. (9) for constant temperature ($T = 81$ mK and resistance $R = 20\%\ R_n$). This suggests that the derivative of a measured $I_C(B)$ at a constant temperature can be used as a good approximation to the expected β.

whereas $\beta(B_{ex})$ oscillates with $\partial I_C(B_{ex})/\partial B_{ex}$. Assuming $I_{C+}(B) = I_{C-}(-B)$, it follows that $\alpha_+(B_{ex})$ and $\beta_+(B_{ex})$ for positive bias direction will equal $\alpha_-(-B_{ex})$ and $\beta_-(-B_{ex})$ for the negative bias direction. $\beta(B_{ex})$ and $\alpha(B_{ex})$ for both bias directions are presented in Figs. 17(b) and 17(c), respectively. Since $\beta(B_{ex})$ and $\alpha(B_{ex})$ have different functional forms, by engineering a device with a different self-field factor (g_I) it is theoretically possible to change β relative to α. A reduction in β is potentially beneficial because it reduces the detector Johnson noise and thus improves the detector energy resolution (Eq. (7)). Further details of this potential optimization are reported elsewhere.[38]

3. Case 3: $g_I = 0$, $g_T \neq 0$

Next, we introduce a temperature dependent shift, of the form $\Delta B = g_T(T - T_{C0})$, to the $I_C(T,B)$ (Case 3: $g_I = 0$, $g_T \neq 0$). In Figs. 18(a) and 18(b), we present the calculated $I_C(T,B)$ and $R(T,I)$, respectively, assuming $g_T = 0.2\ \mu$T/mK. In the same way that a current dependence to I_C will introduce features in $R(T,I)$ at constant I, a temperature dependent shift will introduce features along lines at constant T. Essentially, this is very similar to Case 2 described above but now these features appear in α as opposed to β. Thus, we briefly review the key findings. Since we assume $g_I = 0$, $\beta(R/R_n)$ will be the same as Case 1 and β will be independent of applied field for constant resistance. However, α will be significantly modified by the additional derivative term $g_T T/I_C \partial I_C/\partial B$. This is the same derivative term that appears in Eq. (16) for β only now it depends upon $g_T T$. Figure 19 shows $\alpha(R/R_n)$ for a series of different applied fields. The discontinuity at 80% R_n for $B = 0.0\ \mu$T corresponds to the first minimum in the $I_C(B)$. This shifts to lower in the transition as the applied field is changed. The discontinuities are in the direction of an increase in α with decreasing R/R_n, opposite to that of β for the example presented previously (see Fig. 16).

The field dependence of α will also now be dominated by the second derivative term in Eq. (15) and α will have the same form as β in the Case 2 example (in both cases this will essentially take the form of $\partial I_C(T,B)/\partial B_{ex}$). Figure 20(a) shows $\alpha(B_{ex})$ for the same three examples of I_{bias} presented in Fig. 17(a). Fig. 20(b) shows $\alpha(B_{ex})$ for both positive and negative bias directions. Since the $I_C(B)$ shifts linearly with temperature (corresponding to $B_{ex} = g_T T$), the peak $\alpha(B_{ex})$ will be similarly offset.

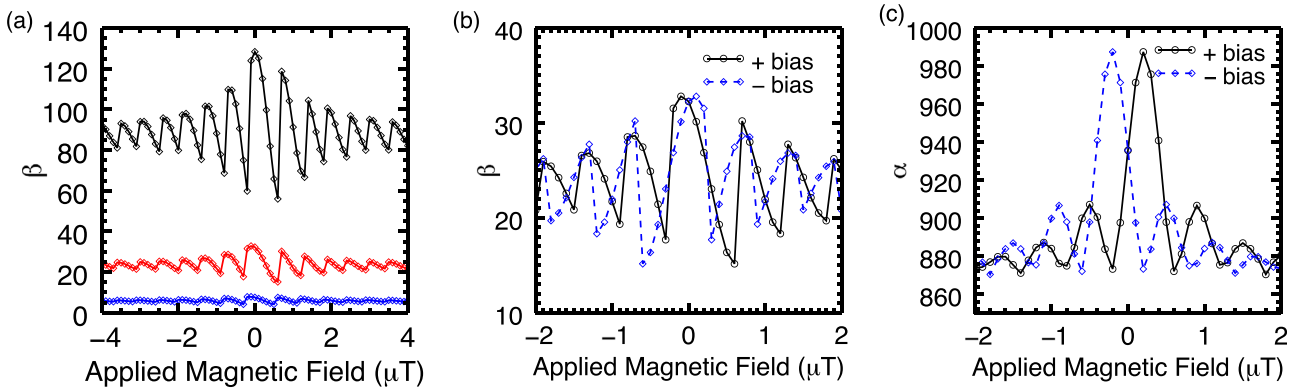

FIG. 17. (a) β is presented as a function of applied field for three different constant $I_{bias} = 284$, 363, and 483 μA (top, middle and bottom traces, respectively), at zero applied field. These correspond to $R \approx 10$, 20, and 37% R_n, respectively. The data are for Case 2 ($g_I = 5\ \mu$T/mA, $g_T = 0$). The shape $\beta(B_{ex})$ is dominated by the term $g_I x_i \partial I_C(T,B)/\partial B$ in Eq. (16). (b) This plot shows β as a function of applied field for both positive and negative bias directions for $I_{bias} = 363\ \mu$A ($R = 20\%\ R_n$). This illustrates the symmetry around zero field consistent with the $I_C(B)$. (c) α is presented as a function for applied field for both positive and negative bias directions. In this example, $\alpha(B_{ex})$ has a different functional form and phase to $\beta(B_{ex})$.

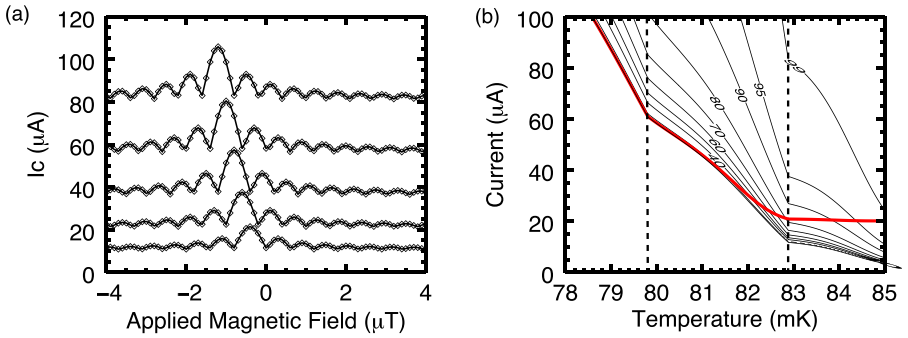

FIG. 18. (a) Calculated $I_C(B)$ for Case 3 ($g_I = 0$, $g_T = 0.2\,\mu$T/mK) for T_b in the range 79–83 mK (in 1 mK increments in order of decreasing I_C). (b) Calculated R(T,I) surface using the $I_C(B)$ for zero externally applied magnetic field. Plotted on the surface are contours of constant percentage R/R_n (thin black lines). Also shown is the bias path defined as the resistance where the bias power is equal to power flow to the heat bath (thick red line). The dotted lines indicates the intersection with the first two minima in the $I_C(B)$ at a temperature of $T = B/g_T = 82.9$ mK and 79.8 mK, respectively.

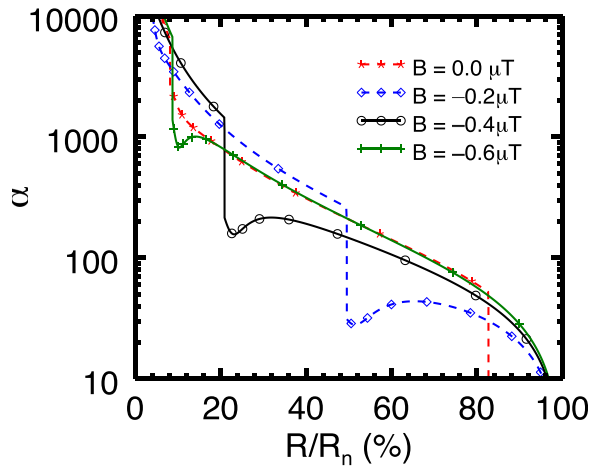

FIG. 19. Presented is the calculated α as a function of R/R_n for four different applied magnetic fields (as indicated on the Figure). The discontinuities in $\alpha(R/R_n)$ arise from discontinuity in $\partial I_C(T,B)/\partial B$ at the minima in the $I_C(B)$. As the externally applied field is changed, the position of these features will move to a different part of the transition.

4. Case 4: $g_I \neq 0$, $g_T \neq 0$

As a final test case, we introduce both a T dependent phase and I dependent self-field $\Delta B = g_I I + g_T(T - T_{C0})$ (Case 4: $g_I \neq 0$, $g_T \neq 0$). In this scenario, the features in the $I_C(B)$ will manifest with both a T and I dependence in the $R(T,I)$ surface. Figs. 21(a) and 21(b) show the $I_C(T,B)$ and $R(T,I)$ surface, respectively, for $g_I = 2.5\,\mu$T/mA, $g_T = 0.14\,\mu$T/mK. Note that in this combination, $\Delta B(I)$ is in the opposite direction to the $\Delta B(T)$. Through Eqs. (15) and (16), this results in oscillations in $\alpha(B_{ex})$ and $\beta(B_{ex})$ that are in phase with each other and dominated by the derivative terms (see Fig. 22(a)). If the current and temperature dependence were in the same direction then it follows that the oscillations would be out of phase with each other. This is modeled in Fig. 22(b) which shows $\alpha(B_{ex})$ and $\beta(B_{ex})$ for $g_I = -2.5\,\mu$T/mA and $g_T = +0.14\,\mu$T/mK. As with Cases 2 and 3, the larger g_I or g_T the larger the magnitude of the oscillation in β or α, respectively. As a function of R/R_n, both α and β will now have features which are correlated and thus occur at the same resistance within the transition. This is presented for both examples in Fig. 23.

Since α and β both depend upon derivatives of I_C with respect to both temperature and current, the exact form of $I_C(B)$ is very important for determining their field and resistance functionality. Although Eq. (10) demonstrates the basic principles of this model, it is not a perfect representation of the complex temperature and field evolution of the measured I_C data. The minima in Eq. (10) used to calculate the $I_C(B)$ results in discrete changes in the derivative whilst the maxima are more rounded and result in more subtle changes in transition shape. Thus, slight differences in these features have the potential to make a large difference in α and β. For example, a sinusoidal $I_C(B)$ would result in a similar sinusoidal α and β, simply phase shifted ($d(\sin\theta)/d\theta = \sin(\theta + \pi/2)$). As a function of R/R_n α and β would change gradually without the discrete jumps that appear in the examples presented here.

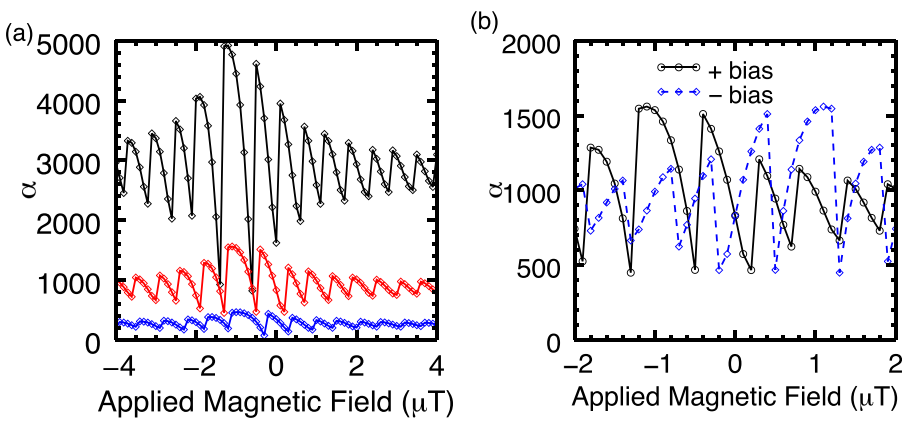

FIG. 20. (a) α is presented as a function of applied field for three different constant $I_{bias} = 284$, 363, and 483 μA (top, middle, and bottom traces, respectively), at zero applied field these correspond $R \approx 10$, 20, and 37% R_n, respectively. The shape of $\alpha(B_{ex})$ is dominated by the term $\partial I_C(T,B)/\partial B$ in Eq. (15). (b) This plot shows α as a function of applied field for both positive and negative bias directions $I_{bias} = 363\,\mu$A ($\approx 20\%$ R_n).

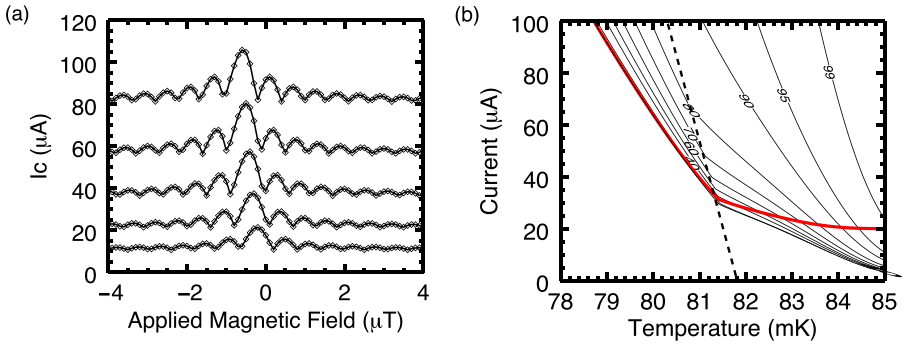

FIG. 21. (a) Calculated $I_C(B)$ for Case 4 ($g_I = +2.5\ \mu T/mA$, $g_T = +0.14 \mu T/mK$) for T_b in the range 79–83 mK (in 1 mK increments in order of decreasing I_C). (b) Calculated R(T,I) surface using the $I_C(B)$ for zero externally applied magnetic field. Plotted on the surface are contours of constant resistance (thin black lines). Also shown is the bias path defined as the resistance where the bias power is equal to power flow to the heat bath (thick red line). The dotted line indicates the intersection with the first minimum, which now has both an I and T dependence.

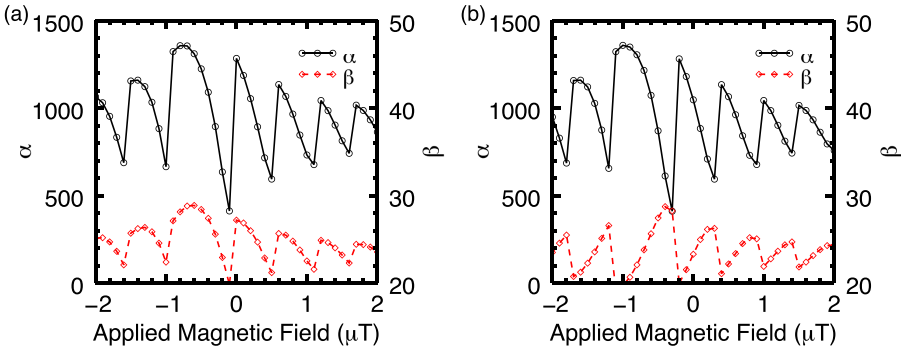

FIG. 22. Presented are α (left axis) and β (right axis) as a function of applied field for (a) $g_I = 2.5\ \mu T/mA$, $g_T = 0.14\ \mu T/mK$ and (b) $g_I = -2.5\ \mu T/mA$, $g_T = 0.14\ \mu T/mK$. Changing the polarity of g_I changes the phase of the β oscillations with respect to α.

VI. MEASUREMENTS OF THE RESISTIVE TRANSITION

A. Field dependence of α and β

To provide comparison with the predictions of the model described in the Sec. V, we have carried out measurements of α and β as a function of both B_{ex} and R/R_n for different bath temperatures. We use the approach by Lindeman *et al.* and measure the frequency dependent complex impedance of the TES $Z(f)$[39] in the range 10 Hz–5 kHz. Knowledge of the total device heat capacity C and the thermal conductance to the heat bath G_b, as well as the bias and readout circuit parameters, allows us to fit the real and imaginary complex impedance using a small signal TES microcalorimeter model for α, β, and R/R_n. Further details of modeling and example fits to experimental data for our Mo/Au devices can be found in Refs. 19 and 27 and will not be revisited here. In these particular devices, the heat capacity is dominated by the electronic contribution from the Au absorber. The total heat capacity is measured from the decay time of average measured x-ray pulses while operating with a bath temperature slightly above the abrupt on-set of superconductivity. The use of a small ($\sim$1 μA) TES bias current ensures that the self-heating is negligible and the TES temperature is the same as the bath temperature. In this régime, the electro-thermal feedback is negligible and the pulse decay time (Eq. (2)) is governed by the intrinsic thermal response ($\tau = C/G_b$). The thermal conductance, $G_b = 160 \pm 8$ pW/K, is calculated from the measured power required to bias the TES in the transition as a function of the bath temperature.

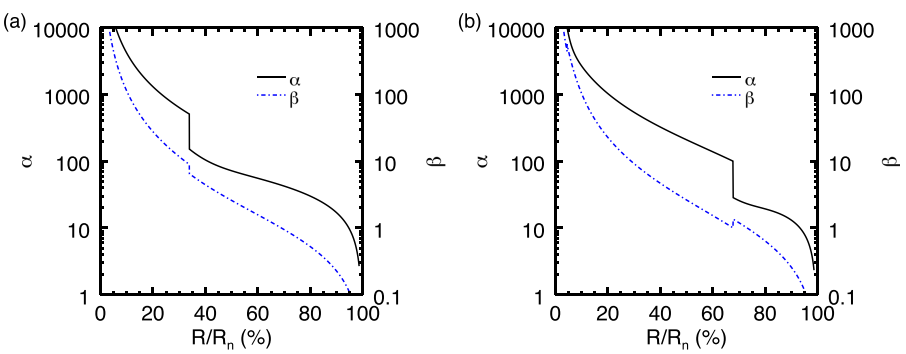

FIG. 23. Presented are α (left axis) and β (right axis) as a function R/R_n for (a) $g_I = 2.5\ \mu T/mA$ and $g_T = 0.14\ \mu T/mK$ and (b) $g_I = -2.5\ \mu T/mA$, $g_T = 0.14\ \mu T/mK$.

We then find $C = 1.52 \pm 0.08$ pJ/K, consistent with the value expected from the absorber geometry (1.4 pJ/K) and a small contribution from the TES (~0.1 pJ/K). The uncertainty in α and β is dominated by systematic errors arising from uncertainties from other parameters used in the model (such as C, G_b, L_{in}), which we estimate to be ~5%. Statistical errors are estimated to be ~1%.

Due to the experientially intensive nature of these measurements, it is not practical to map out the full $R(T,I,B)$ parameter space. Measurements were focused in the lower half of the resistive transition since this is typically where the best signal-to-noise performance is achieved for these types of devices.[27,29] Figure 24(a) shows the best-fit values of α and β from the measured $Z(f)$ as a function of (R/R_n) up to 50% R_n. The results show that the α values typically reach a peak of 500–1000 and β values of 10–20 at bias points of 5–10% R_n. The data show how the changing magnetic field changes the shape of $\alpha(R/R_n)$ and $\beta(R/R_n)$. This is most clearly illustrated in the peak in α and β that appears at different R/R_n for different applied fields. The maximum in α and β occurs at the same R/R_n for a given applied field, suggesting that α and β are correlated. From the modeling presented in Sec. V, this is indicative of Case 4, where there exists both a T and I dependence to the shift in I_C. This results in generally correlated features in α and β as a function of B_{ex} and R/R_n (as is illustrated in Figs. 22 and 23). The apparent discontinuities in α and β as a function of R/R_n are also predicted for the non-zero g_I and g_T case (Fig. 23, for example). The data show that for decreasing R/R_n, α and β reach a peak before jumping to lower values, however this specific behavior is difficult to exactly recreate in the model where the discontinuities are either in opposing directions for α and β (Fig. 23(a)) or both in the direction of increasing α and β with decreasing R/R_n (Fig. 23(b)).

To provide a simple basis for comparison with the measured $\beta(R/R_n)$, we also show the pre-factor in Eq. (16) $(R_n/R)^2 - 1$ (which only in the limit of $g_I = 0$ would be expected to provide a realistic functional form for β). This is arbitrarily scaled by the factor 0.1 to align approximately with data points above ~15% R_n. A similar comparison is made with α in Fig. 24(a). In the case of $g_T = 0$, $\alpha = -\beta\, T/I_C\, \partial I_C/\partial T$. We calculate $\partial I_C/\partial T$ from the measured $I_C(T)$ assuming $B_{ex} = 0$, and the TES temperature is calculated from Eq. (17) (and is shown in Figure 24(b)). The same arbitrary scale factor of 0.1 is incorporated to compare the modeled data to the measurement.

The need for an arbitrary scale factor of 0.1 for both α and β is not consistent with the model outlined in Sec. V. Even though an order of magnitude difference between β for $g_I = 0$ and $g_I \neq 0$ is possible, $\beta(B_{ex})$ should however vary around a mean value that is approximately consistent with the $g_I = 0$ case. Thus, it is more likely that the results are systematically smaller than predicted due to inadequacies of the one-dimensional RSJ model presented. One interpretation could be that $T/I_C\, \partial I_C/\partial T$ may be the correct term for calculating α, but the pre-factor $(R/R_n)^2 - 1$ could be incorrect, since this term is common to both α and β. Given the simplicity of the one-dimensional model presented and the complexity of the actual device geometry, it is perhaps not surprising there are discrepancies. This may be a result of the effects of non-equilibrium superconductivity or incorrect assumptions in the derivation of the RSJ model, such as the sinusoidal current-phase relation and uniform current density distribution, for example. The resistance versus temperature measurements for devices similar to the ones reported here, but with a stem configuration that transverses the whole width of the sensor (as opposed to the "T"-Stem depicted in Fig. 4), showed a significantly broadened transition width that was attributed to charge imbalance from supercurrent to quasi-particle recombination across the stem feature.[16] Such physical processes may also play a significant role in determining the transition width, and therefore α and β, for the device geometry reported here.

Figure 25 shows $\alpha(B_{ex})$ and $\beta(B_{ex})$, respectively, as a function of applied magnetic field measured for two examples of different constant applied I_{bias}. For the top and bottom panels, the data correspond to $I_{bias} = 382\ \mu$A and $I_{bias} = 290\ \mu$A, respectively (which are ~15.3% R_n and ~7.5% R_n, respectively, at $B_{ex} = 0$). The three vertical lines correspond to the fixed fields at which the data in Fig. 24 are

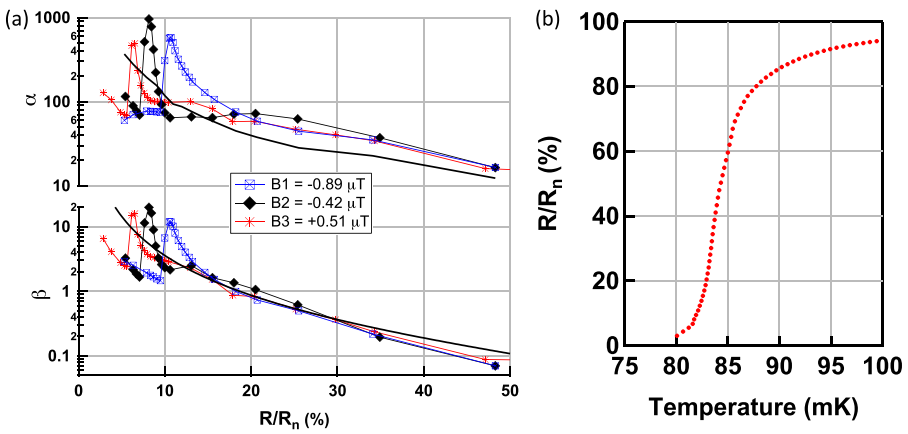

FIG. 24. (a) α (top) and β (bottom) as a function of R/R_n for three different applied fields. Data points are connected to provide a guide to the eye. Each data point is calculated from the best fit Z(f). The solid line (no symbols) provides a comparison to the data. For β, this corresponds to the pre-factor in Eq. (16), $0.1((R_n/R)^2 - 1)$ and for α Eq. (15), $0.1((R_n/R)^2 - 1)T/I_C\partial I_C(T)/\partial T$. The factor 0.1 is an arbitrary scale factor introduced for ease of comparison. (b) R/R_n as a function of the calculated TES temperature along the bias path (Eq. (17)) for approximately zero applied magnetic field.

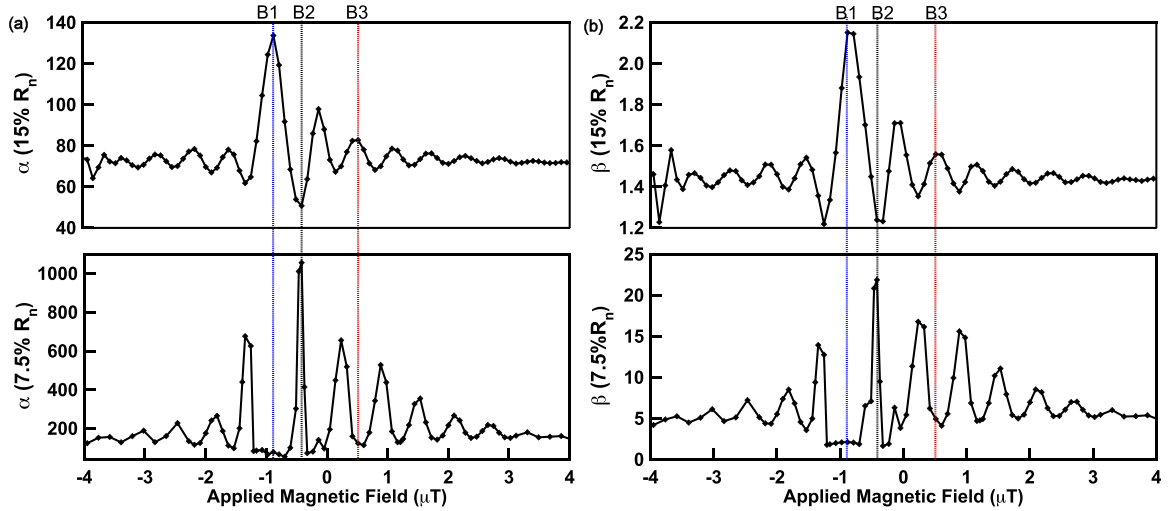

FIG. 25. (a) Best fit α as a function of applied magnetic field for $I_{bias} = 382\,\mu A$, which corresponds to ~15.3% R_n (top) and for $I_{bias} = 290\,\mu A$ corresponding to 7.5% R_n (bottom) at zero applied field. The three vertical lines correspond to the fixed fields at which the data in Fig. 24 is measured. (b) Best fit β as a function of applied magnetic for the same two I_{bias} examples. Data points are connected to provide a guide to the eye.

measured. Since the data are measured at constant applied I_{bias}, as discussed in Sec. V, R/R_n is in general not constant with applied field. For the higher operating point in the transition ($I_{bias} = 382\,\mu A$), $\alpha(B_{ex})$ and $\beta(B_{ex})$ show oscillatory behavior with applied field. A peak in both $\alpha(B_{ex})$ and $\beta(B_{ex})$ occurs at $B_{ex} = -0.89\,\mu T$ and the width of this oscillation is $\Delta B \sim 0.9\,\mu T$. Away from the central maximum, the average oscillation period is $\Delta B = 0.59 \pm 0.04\,\mu T$. These values closely match the periodicity of the $I_C(B)$ data presented in Sec. IV ($\Delta B = 0.9\,\mu T$ for the central oscillations and $\Delta B = 0.55 \pm 0.02\,\mu T$ elsewhere at $T = 84.4$ mK). As the temperature and current change with bias point, the relative phase of the oscillations is expected to change. For the lower operating point ($I_{bias} = 290\,\mu A$), similar oscillatory behavior is observed however there exists a different phase relative to the higher operating point example. We also note that there is a change in shape to the oscillations as well. The largest maxima are narrower and the variation in amplitude is approximately a factor of 10 (compared with 2 for $I_{bias} = 382\,\mu A$). Figure 26 shows R/R_n as a function applied field determined from the complex impedance data for the two chosen bias points. Some oscillatory behavior in R/R_n is observed but the relative magnitude of the oscillations is significantly smaller than in $\alpha(B_{ex})$ and $\beta(B_{ex})$.

Given the symmetry properties of the measured critical current presented in Sec. IV ($I_{C+}(B_{ex}) \approx -I_{C-}(-B_{ex})$), and the prediction from the modeling that $\alpha_+(B_{ex}) = \alpha_-(-B_{ex})$ and $\beta_+(B_{ex}) = \beta_-(-B_{ex})$, we have measured a subset of the data for both bias directions. This is presented in Fig. 27 for $I_{bias} = 382\,\mu A$. Although there are some deviations, the general phase and magnitude seem to be in agreement with the expected symmetry for the different field and bias directions. Figure 28 shows an expanded view of the same α and β data. Though in general α and β seem in phase, there is a slight systematic phase difference between the two of $\sim 0.07\,\mu T$ which appear in both positive and negative bias directions.

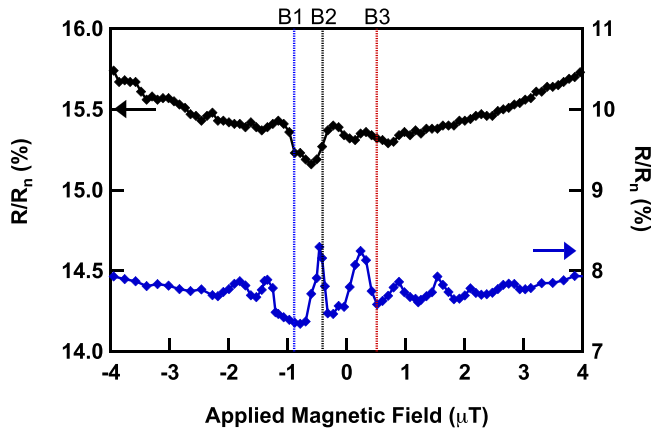

FIG. 26. Fitted bias point percentage (R/R_n) for constant I_{bias} as a function of applied magnetic field. The top line corresponds to $I_{bias} = 382\,\mu A$ (left axis) and the bottom line corresponds to $I_{bias} = 290\,\mu A$ (right axis). Data points are connected to provide a guide to the eye.

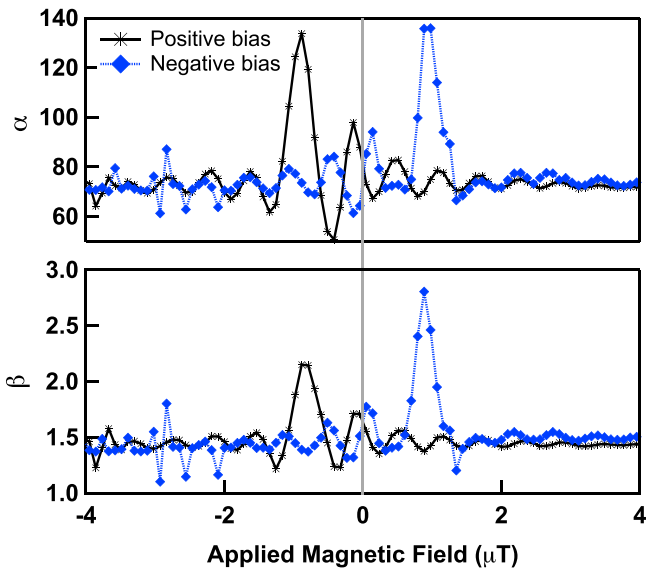

FIG. 27. α (top) and β (bottom) for $I_{bias} = +382\,\mu A$ and $I_{bias} = -382\,\mu A$ bias as a function of applied field. The general features suggest $\alpha_+(B_{ex}) \approx \alpha_-(-B_{ex})$ and $\beta_+(B_{ex}) \approx \beta_-(-B_{ex})$, consistent with the symmetry properties of the measured $I_C(T,B)$.

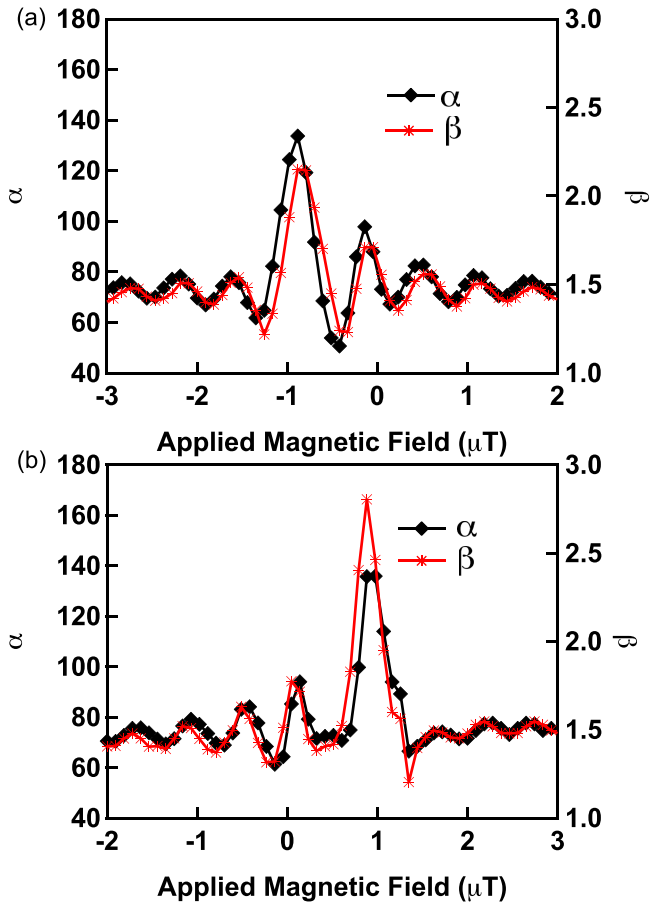

FIG. 28. (a) α (left axis) and β (right axis) for positive bias direction and (b) negative bias directions. The data indicate a small phase difference of $\sim$0.07 μT between α and β.

Since α and β are derived from the same $Z(f)$ for each measured data point, it is not possible to introduce a systematic offset experimentally. Thus, this is believed to be physical in origin. This might result from the two different derivative terms that combine in Eq. (15) for α, which can have a different phase relation with each other (as opposed to only one for β). For the $I_{bias} = 290\,\mu$A data, there is no discernable phase difference between α and β to within the measurement accuracy.

Increasing the bath temperature of the ADR, T_b, reduces the required joule power to operate the device in the transition (Eq. (17)). Consequently, the bias path along the $R(T,I)$ surface will occur at a higher temperature and lower current. Thus, changing T_b provides a means to probe a different part of the $R(T,I)$ surface. Presented in Fig. 29 are measurements of $\alpha(R/R_n)$ and $\beta(R/R_n)$ for $T_b = 77$ mK. Also presented is $\alpha(B_{ex})$, $\beta(B_{ex})$, and $R/R_n(B_{ex})$ for $I_{bias} = 225\,\mu$A. In general the observations are very similar to the previous two examples except for changes in magnitude and phase of the oscillations.

In order to examine the relation between the measured α and $I_C(T,B)$ for the three example data sets, we plot all three $\alpha(B_{ex})$ data sets on Fig. 30(a) (labeled 1–3). For comparison with $\partial I_C/\partial B_{ex}$, the $\alpha(B_{ex})$ data are vertically offset and arbitrarily scaled. In the simple modeled predictions from Sec. V, $\alpha(B_{ex})$ or $\beta(B_{ex})$, can be compared directly with $\partial I_C(B)/\partial B_{ex}$ for a fixed temperature (see, for example, Fig. 16(b)). Thus, we plot $\partial I_C/\partial B_{ex}$ calculated from directly differentiating the measured $I_C(B)$ data presented in Fig. 6(b), for $T = 80.9$ mK, 81.9 mK, and 83.0 mK. This is equivalent to the last term in Eq. (15) for α, which under the assumption of constant T and constant R/R_n can be used to illustrate the expected behavior in $\alpha(B_{ex})$. These temperatures were chosen because they correspond closely to the TES temperature under bias for the three $\alpha(B_{ex})$ examples. The data are vertically offset to approximately align with the $\alpha(B_{ex})$ data. The TES temperatures (calculated from Eq. (17)) corresponding to the three $\alpha(B_{ex})$ measurements are presented in Fig. 30(b). These differ by less than $\sim\pm0.5$ mK from the temperatures at which $\partial I_C/\partial B_{ex}$ in Fig. 30(a) was measured. Compared with the simulated examples presented in Sec. V, the measured $\partial I_C/\partial B_{ex}$ oscillations are generally more rounded and symmetric, this in turn results in more rounded $\alpha(B_{ex})$ than the examples in Sec. V. The more abrupt jumps in the transition parameters, around the largest peaks in $\alpha(B_{ex})$ (for the data labeled 1 and 3 in Fig. 30(a)), correspond to the same abrupt discontinuities measured as a function of R/R_n (Fig. 24(a), for example). Although this type of feature is a prediction from the model, given the rounded $\partial I_C/\partial B_{ex}$ features it is not possible to conclude that these abrupt changes are necessarily of the same mechanism presented in the modeled examples (as illustrated in Fig. 23). Further measurement would be required at a variety of different TES temperatures within the transition to comprehensively map the transition parameters to understand further how specific features in the $R(T,I)$ correlate to the measured critical current. Somewhat surprisingly, given the uncertainty in the temperature and the approximations outlined above, the periodicity and phase for the three examples of $\alpha(B_{ex})$ agree rather well with $\partial I_C(B)/\partial B_{ex}$. As the TES temperature decreases for the three examples, the phase of $\alpha(B_{ex})$ shifts away from zero applied field. The maximum in $\partial I_C(B)/\partial B_{ex}$ shifts by $\sim$0.63 μT from 83.0 mK to 80.9 mK. Although the shape of the measured $\alpha(B_{ex})$ is not identical between temperatures, the phase shifts by approximately the same amount consistent with expectation. The measured $\alpha(B_{ex})$ at constant I_{bias} also includes the effect of resistance and temperature changing. The superposition of both temperature and resistance changing can result in distortions of the measurements of $\alpha(B_{ex})$ and may in part explain why the shape is different between the $\partial I_C(B_{ex})/\partial B_{ex}$ and $\alpha(B_{ex})$.

B. Response to X-rays

Through Eqs. (1) and (2), the magnetic field dependence of the small signal transition parameters α and β affects ΔI and τ_{etf}. In this section, we present measurements of the pulse ΔI and τ_{etf} as a function of applied magnetic field and bias point and discuss the implications for array uniformity and for stability in time varying fields. A ^{55}Fe electron capture source is used to illuminate the detector area with Mn-Kα x-rays at an energy of 5898 eV. Approximately 100 x-ray events are logged and averaged. ΔI is determined from the maximum value of each record and τ_{etf} is determined from an exponential fit to the pulse decay time. The estimated

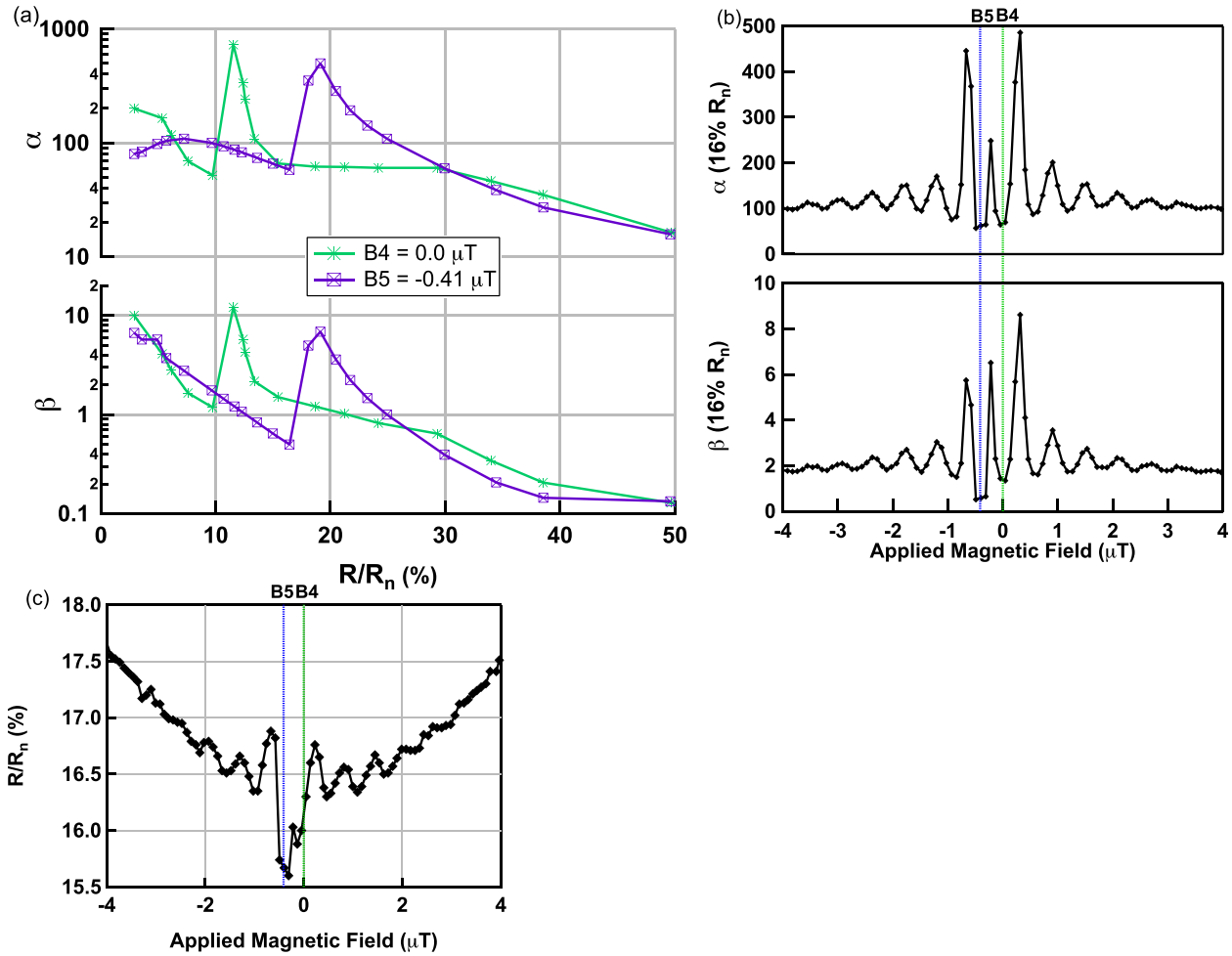

FIG. 29. (a) The best fit α (top) and β (bottom) as a function of R/R_n for two different applied magnetic fields. The bath temperature is 77 mK. (b) This figure shows the best fit α (top) and β (bottom) as a function of applied magnetic field for $I_{bias} = 225\ \mu A$. (c) Best fit R/R_n as a function of applied field. The two vertical lines in both (b) and (c) correspond to the fixed fields at which the data in (a) were measured. Data points are connected to provide a guide to the eye.

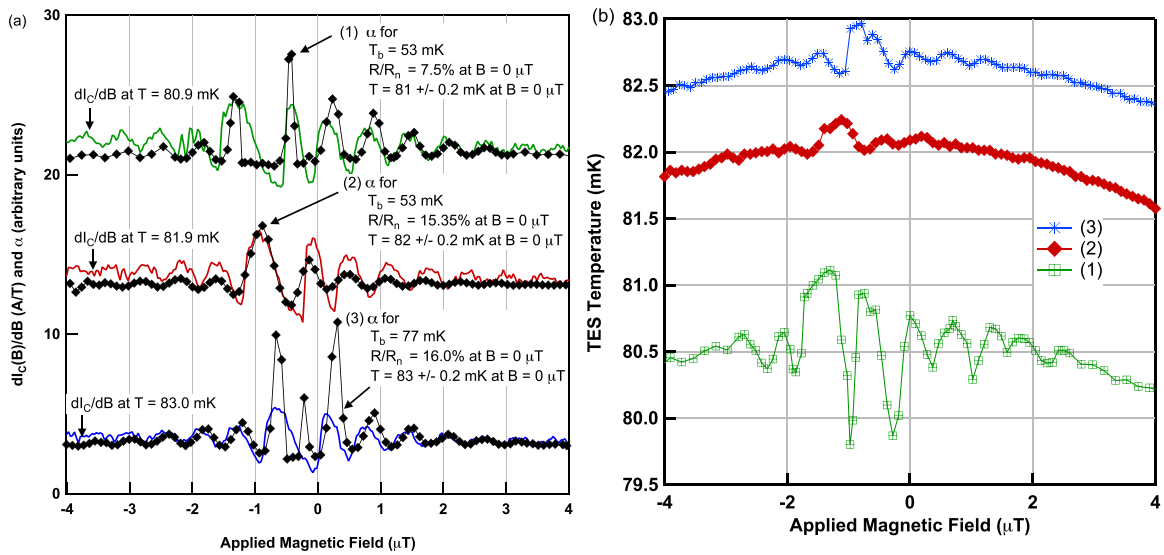

FIG. 30. (a) Measured $\alpha(B_{ex})$ for three different measurement conditions (labeled 1–3) as indicated in the figure. Each data set is vertically offset and arbitrarily scaled. Also shown is $\partial I_C(B)/\partial B_{ex}$ calculated from the measured $I_C(B)$ presented in Fig. 6(b) for $T = 80.9$ mK, 81.9 mK, and 83 mK. Each data set is vertically offset to approximately align with $\alpha(B_{ex})$. These temperatures were chosen because they correspond approximately to the TES temperature under bias for the three $\alpha(B_{ex})$ examples. (b) TES temperature under bias (calculated from Eq. (17)) as a function of applied field. The data correspond to the three $\alpha(B_{ex})$ examples presented in (a) (labeled 1–3).

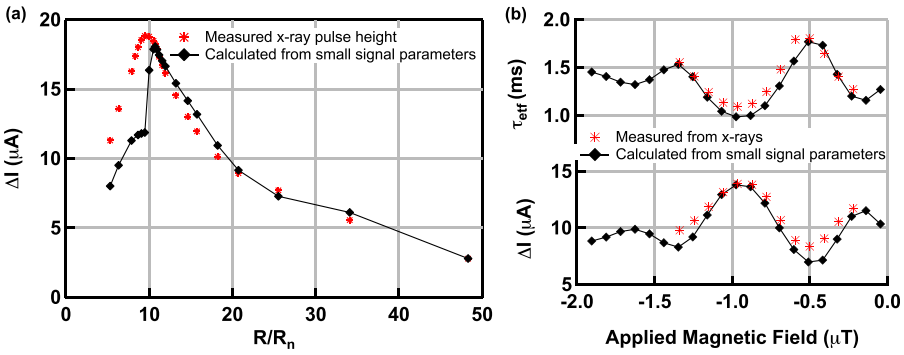

FIG. 31. (a) Measured pulse height, ΔI, as a function of R/R_n for constant applied field −0.89 μT (B1) and (b) decay time, τ_{etf} and ΔI as a function of applied magnetic field for constant $I_{bias} = 382\,\mu A$. Shown for comparison are ΔI and τ_{etf} calculated using the small signal transition parameters α and β (shown previously in Figs. 24 and 25).

statistical error in the measured ΔI is $\sim\pm 0.2\,\mu A$ and τ_{etf} is $\sim\pm 2\,\mu s$.

Fig. 31(a) shows ΔI as a function of R/R_n for fixed applied field (B1 = −0.89 μT). Fig. 31(b) shows ΔI and τ_{etf} as a function of the applied field for $I_{bias} = 382\,\mu A$. Also, shown on Fig. 31 is the calculated ΔI and τ_{etf} using the measured transition parameters α and β from Figs. 24 and 25 and a small signal detector model,[23] which in the limit of $L_{in} = 0$ and $R \gg R_S$ reduces to Eqs. (1) and (2), respectively. Above $\sim 10\%\ R_n$, the measured ΔI agrees well (to within ∼10%) with that predicted from the small signal detector parameters. However just below 10% R_n, the measured x-ray pulse heights are ∼55% larger than that predicted from the model. This is attributed to non-linearity in the detector response. In these relatively large heat capacity devices, we estimate that a photon energy of ∼6 keV will transverse only ∼5–10% of the transition. However, since α and β can change by an order of magnitude for only a few $\%R_n$, when biased below 10% R_n, a 6 keV x-ray event may sample a higher resistance part of the transition where α and β are very different than at the quiescent bias point. The x-ray will not sample the identical path in $R(T,I)$ space as the bias trajectory since, when the photon is absorbed, the electro-thermal feedback results in a decrease in I as T and R increase. However, the observed enhancement of the pulse height in these measurements is suggestive that the pulses intersect similar features in α and β as measured along the bias path. The non-linearity is further illustrated by the average measured pulse shapes (shown in Fig. 32(a)), which show two exponential components to the measured decay time constants $\tau_1 = 1.06$ ms and $\tau_2 = 1.62$ ms (for events measured at $R = 8.6\%\ R_n$) compared with the single exponential of the small signal model. The faster time constant τ_1 is consistent with sampling a higher resistance part of the transition, where the detector response is faster, whereas τ_2 matches the small signal calculation for that bias point.

As a function of applied field, α and β combine such that predicted ΔI and τ_{etf} oscillate out of phase with each other in close agreement (at a level of ∼10%) with the measured results (Figs. 31(b) and 32(b)). The discrepancy could also be a result of non-linearity in the detector response (but a much lower level than discussed above) or some systematic errors from the small signal model parameters.

This dependence of sensor responsivity on magnetic field has implications for device performance and calibration. Non-linearity in the detector responsivity with energy can result in uncertainty in the absolute energy scale and make higher demands on calibration. Spatially varying static fields over an array can result in pixel-to-pixel non-uniformity. Uniformity is particularly important for time-domain multiplexed (TDM) SQUID readout as proposed[11] for kilo-pixel arrays. This requires the common biasing of many pixels thus it is important the arrays have sufficient uniformity such that every pixel has the optimal performance.

Time varying fields can result in degradation in energy resolution over time due to variations in gain. In our laboratory experiments, variations in gain of the order ∼1% over long time scales (>10 minutes) can be removed by gain correction algorithms and no significant degradation in resolution is observed. However, variations over shorter,

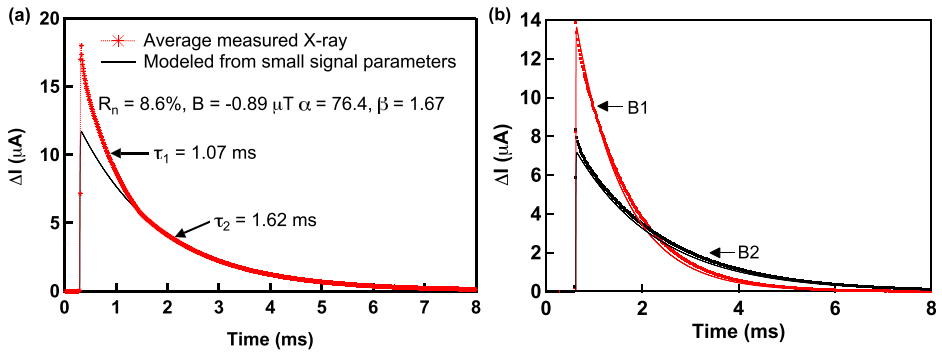

FIG. 32. (a) Comparison of calculated and measured pulse shape for R = 8.6% R_n at B = −0.89 μT (B1). The measured x-ray has a second decay time constant and larger than expected pulse height compared with that calculated from the small signal detector model. (b) Average measured Mn-Kα x-ray events (dots) for $I_{bias} = 382\,\mu A$ for two different magnetic fields of −0.89 μT (B1) and −0.42 μT (B2). The solid lines are the calculated pulse shapes from the small signal detector model. In these examples, the measured and calculated pulse shape agree well.

pulse-to-pulse time scales, which cannot be accurately tracked, have the potential to degrade resolution. Using the maximum pulse shape variation with field from Fig. 31(b), we estimate a field dependence of the measured 6 keV line of 1 eV per 125 pT change in the magnetic field. Thus, a 125 pT rms fluctuation in magnetic field would result in a 1 eV rms broadening in the measured energy resolution. Alternatively, an uncorrected linear drift of 433 pT would result in a 1 eV rms broadening (since the rms contribution of a drift from –A/2 to + A/2 is A/sqrt(12)). This type of analysis can be used to set the magnetic field environment requirements for the various applications of TES arrays. Operating closer to the peak in $\alpha(R/R_n)$ (around 7.5% in this example) is detrimental to performance since it introduces a much greater level of field sensitivity as well as non-linearity in the detector response to x-rays and non-stationary noise.[40]

C. Noise and energy resolution

Having derived α and β from $Z(f)$, we can calculate the theoretical noise spectral density of the TES and compare it with the measured noise. We calculate the average current noise spectral density, $\sqrt{\langle |N(f)|^2 \rangle}$, from the Fourier transforms of approximately 500 randomly triggered noise traces. The same model used to fit $Z(f)$ is used to calculate the expected current noise spectral density. The main noise terms (as discussed in Sec. II) included are TES phonon noise (Eq. (4)) and TES Johnson noise (Eq. (5)). In addition, a white current noise from the SQUID electronics and analog-to-digital converter (ADC), which varies from ~10–20 pA/$\sqrt{\text{Hz}}$ depending upon the experimental conditions, is included. The Johnson noise from the shunt resistor is also included in the model but is not a significant contribution to the total noise. The total calculated noise spectral density is then compared with the measured data. The term ϑ^2 in Eq. (5) is set to zero, thus M^2 may include contributions from unknown higher order correction terms in the Johnson noise (which may exhibit additional dependences upon α or β), as well as any other unrelated sources of noise. The unexplained noise factor M^2 is fitted as a free parameter in the model. We estimate the errors in M^2 are <10% due to statistics in the fitting, systematic errors in the small signal transition parameters used in the model and uncertainty in the assumed level of the readout noise. We note that in these measurements, we also found an additional noise component believed to be due to long wavelength radiation creating photon shot noise. This has the same functional form as the phonon noise to the bath and was fitted as an additional parameter in the model. This was found to be 0.77 ± 0.07 times the magnitude of the phonon noise and is independent of detector operating parameters, consistent with previous observations. This has been shown to arise from stray thermal power radiating through the aluminized Mylar x-ray windows on the cold-stage and is not an intrinsic detector noise source.[12] Figure 33 shows the measured and calculated noise for one example described in the caption.

Figure 34(a) shows the calculated α and β as a function of bias point for a single applied field (B1). Note these are the same data as shown in Fig. 24 for an applied magnetic field of $-0.89\ \mu$T (B1). Each data point is color and symbol coded to correspond to the same data points shown in Fig. 34(b). Shown in Fig. 34(b) is $(1+2\beta)(1+M^2)$ as a function of the factor $(1+2\beta)$ that accounts for first order expansion term in the Johnson noise. The solid black line corresponds to $M^2 = 0$, thus data points that fall on this line have no additional unexplained noise contributions. Low in the transition (square symbols), where $\alpha < 100$ and $\beta > 1$, we find that $M^2 \sim 0$. As bias point resistance is increased, we hit the sharp excursion in both α and β at about 10% R_n and correspondingly see a rapid increase in unexplained noise (triangle symbols) to a maximum of $M^2 \sim 15$. As α and β decrease at higher bias points the noise also decreases, returning to $M^2 \approx 0$ at 20% R_n (circle symbols). The fact that different noise levels can exist for the same β value is evidence that the additional noise is not solely dependent upon β, and β cannot solely be used as a reliable predictor of the noise. This is further illustrated in Fig. 35(a), where as well as plotting the B1 data shown in Fig. 34, we also add the noise data corresponding to the applied magnetic field ~0.51 μT (B3). The same approximate scaling is observed in these data, however, because the peak excursion in α and β is now shifted to lower bias points in the transition, the noise occurs at different β values. Fig. 35(b) then shows the noise data at 0.0 μT (B4) and $-0.41\ \mu$T (B5) for $T_b \approx 77$ mK, which corresponds to the α and β data from Fig. 29(a) (note that B5 noise data in Fig. 35(b) are more coarsely sampled than the α and β data in Fig. 29(a)). In these examples the α, β and noise excursion occurs higher up the transition compared with the previous data.

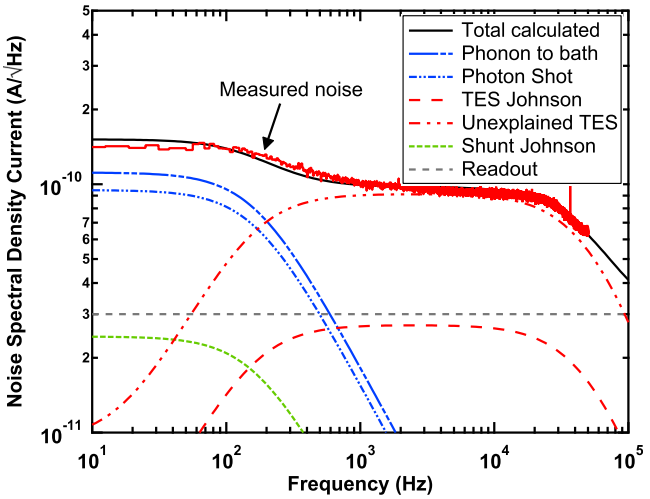

FIG. 33. Comparison of the measured current noise spectral density with the calculated noise using the small signal detector parameters. Shown are the individual noise components that add in quadrature to give the total noise. The measured data correspond to $B = -0.89\ \mu$T (B1) and $R/R_n = 10.9\%$. The small signal transition parameters are $\alpha = 506$ and $\beta = 10.2$, and the unexplained noise factor fitted to the data is $M^2 = 11.4$.

Figure 36 shows M^2 as a function of α for all four data sets discussed. The data suggest that M^2 may be correlated with α for $\alpha > \sim 100$, whereas for $\alpha < \sim 100$, $M^2 < 1$ and there exists no significant unexplained noise. Thus, there appear two distinct operational régimes where the noise characteristics are very different. We note that these results seem to be

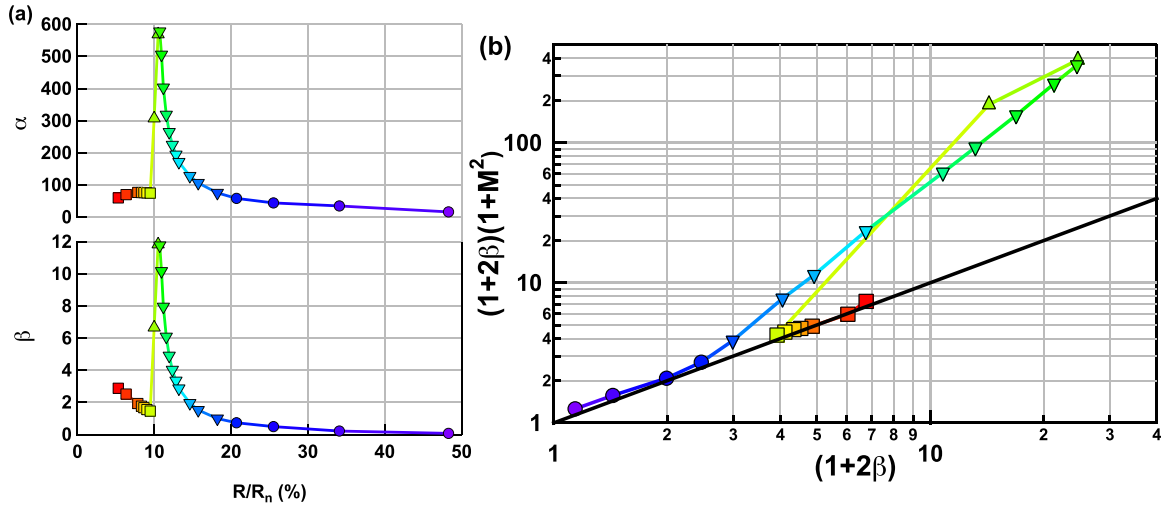

FIG. 34. (a) Calculated α and β as a function of bias point. Note these are the same data as shown in Fig. 24 and correspond to an applied field of $-0.89\,\mu$T (B1). (b) Log-log plot showing the voltage noise factor $(1+2\beta)(1+M^2)$ versus the factor $(1+2\beta)$ that accounts for the first order expansion of the Johnson noise. Each measured data point is color and symbol coded to correspond to the same α and β data points shown in (a). The solid black line corresponds to $M^2=0$.

consistent with noise measurements reported for Mo/Cu bilayer TESs.[41] This scaling is consistently observed for all four data sets in Fig. 36. Further theoretical development is required to determine higher order terms in the non-linear Johnson noise expansion, which may yield terms dependent upon resistance derivatives with temperature.[17] Thermal fluctuation noise[42] from thermal decoupling between parts of the TES has been identified in some higher resistance devices but are not thought to play a significant contribution in our low resistance, high thermal conductance detectors.

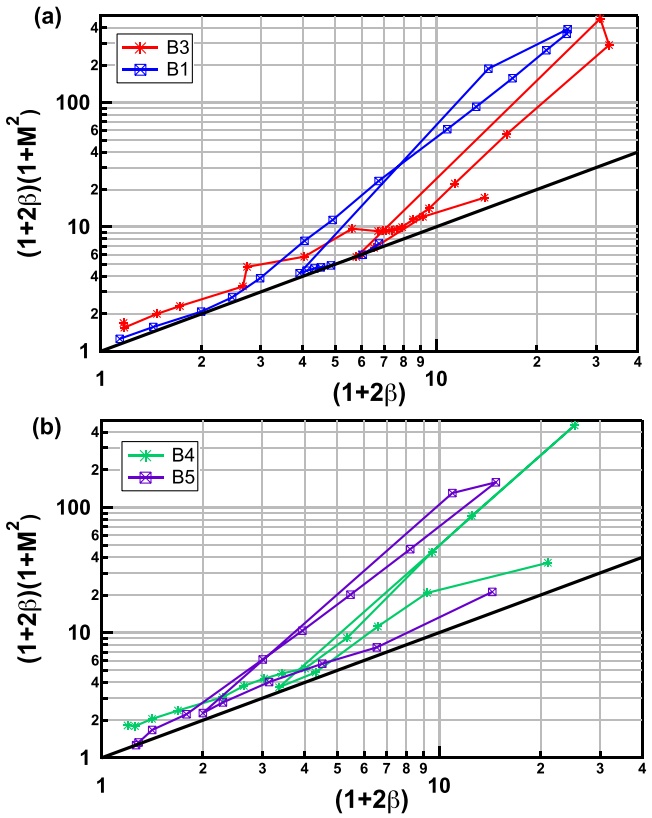

FIG. 35. (a) Log-log plot showing $(1+2\beta)(1+M^2)$ as a function of just the first order expansion term $(1+2\beta)$. These data are measured at 54 mK for an applied magnetic field of $-0.89\,\mu$T (B1) and $-0.51\,\mu$T (B3). (b) These data are measured at $0.0\,\mu$T (B4) and $-0.41\,\mu$T (B5) at 77 mK.

The predicted energy resolution ΔE_{FWHM} is determined from Eq. (6) from the average noise power $\langle|N(f)|^2\rangle$ and the detector responsivity $|S(f)|^2$, which is calculated from the Fourier transform of average measured pulses normalized to a delta-function input of power. Figure 37 shows the predicted ΔE_{FWHM} as a function of R/R_{n} from both the measured signals and calculated from the small signal model (which reduces to Eq. (6) in the limits discussed in Sec. II). The discrepancy between ΔE_{FWHM} inferred from measured data and the small-signal analysis is consistent with the non-linearity in the pulse shape discussed in Sec. V. Below 10% R_{n}, the measured 6 keV x-ray overestimates the small-signal detector responsivity and results in a significantly better predicted ΔE_{FWHM} compared with the small signal model. The dotted line shows the effect of setting $M^2=0$ at all bias points and indicates the region of the transition where the degradation in ΔE_{FWHM} due to non-zero unexplained noise occurs. Figure 38 shows how both M^2 and ΔE_{FWHM} vary with magnetic field. In this specific example, the worst resolution corresponds to both the lowest noise and the smallest pulse height. However, the optimum resolution does not correspond to the maximum in the pulse height, since here M^2 is now close to 3. In fact, the best resolution occurs somewhere in-between, where $M^2\approx 1$ but the pulse height is close to maximum. This complex relation between M^2, α, and ΔE_{FWHM} illustrates a practical difficulty in trying to optimize resolution from applying a magnetic field. It is not possible to simply apply a magnetic field to maximize the signal response to x-rays or alternatively to minimize the unexplained noise. Instead, the optimization depends upon both.

Spectral resolution, as determined from fitting a histogram of filtered x-ray events, has not been comprehensively studied as a function of field and bias point. The spectral resolution was however measured for $I_{\mathrm{bias}}=382\,\mu$A and $B=-0.9\pm0.05\,\mu$T. This corresponds to the maximum in

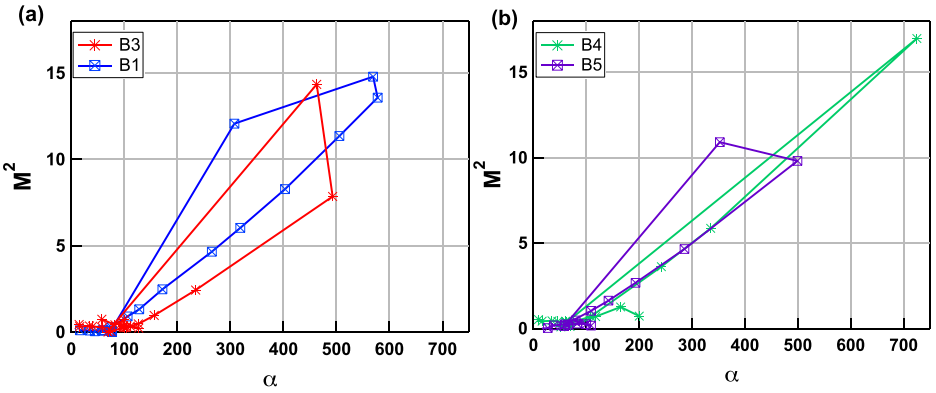

FIG. 36. (a) M^2 as a function of α for applied magnetic fields of $-0.89\,\mu$T (B1) and $0.51\,\mu$T (B3) for $T_b = 54$ mK and (b) for $0.0\,\mu$T (B4) and $-0.41\,\mu$T (B5) at $T_b = 77$ mK.

the pulse height and best predicted ΔE_{FWHM}. The measured spectra resolution was $\Delta E_{\mathrm{FWHM}} = 2.82 \pm 0.15$ eV consistent with the predicted resolution. For the 12 devices reported in Ref. 27, from the same fabricated wafer as tested here, $\Delta E_{\mathrm{FWHM}} = 2.7 \pm 0.15$ eV was achieved for optimized bias points in the range 7–26%R_n. Thus, despite the presence of non-ideal effects in the transition characteristics of these devices, excellent resolution performance has been achieved.

VII. SUMMARY AND CONCLUSIONS

In this contribution, we have examined how the performance of our Mo/Au TES x-ray detectors can be impacted by weak-links behavior. We have carried out comprehensive, high-resolution measurements of the critical current over a broad range in temperature and magnetic field. These measurements reveal Josephson-like oscillations with the applied magnetic field that transition to more Meissner-like behavior at lower temperatures. However, these measurements show significant departure from similar measurements on simple bilayer test structures. This is thought to be due to the presence of additional features (such as noise-mitigation stripes and absorber-attachment stems) introducing spatial inhomogeneity to the superconducting order parameter and current density distribution. This is further complicated by the presence of self-induced magnetic fields generated by current flowing in the electrical bias leads and sensor itself.

We have presented a simple one-dimensional resistively shunted junction model for calculating the TES $R(T,I,B)$ that incorporates the effects of temperature, current, and externally applied, as well as self-induced, magnetic field dependence to the critical current. The important result from this model, despite the simplicity, is the prediction that it is possible to generate complex structure in the resistive transition, such as kinks, discontinuities, and oscillations with applied magnetic field. Thus, this type of behavior should be considered fundamental and generally expected, though the exact manifestation is likely to be highly dependent on the details of the complex three-dimensional geometry of the device. High resolution measurements of the small signal transition parameters, α and β, for three different bias conditions show correlated oscillatory behavior with applied magnetic field consistent with the predictions of the model. Also, shown are

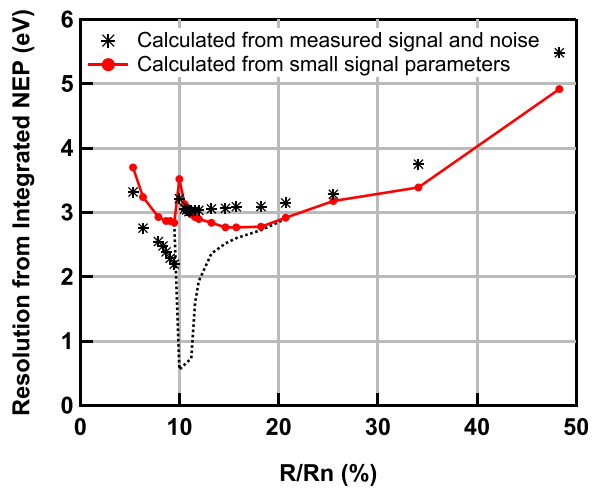

FIG. 37. Predicted ΔE_{FWHM} as a function of R/R_n calculated from the small signal transition parameters compared with that calculated directly from the average measured Mn-Kα x-ray and noise spectral density. The example presented corresponds to $B = -0.89\,\mu$T (B1) and $T_b = 53$ mK. The dotted line is the calculated ΔE_{FWHM} assuming $M^2 = 0$.

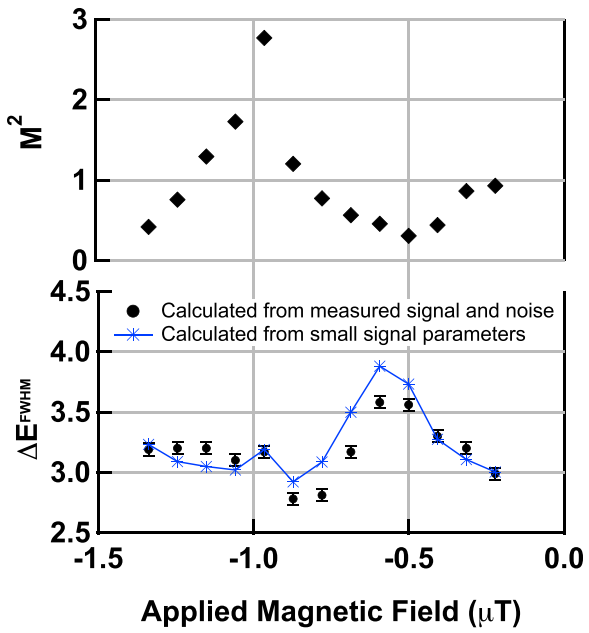

FIG. 38. Best fit unexplained noise parameter M^2 as a function of applied magnetic field (top panel). Also shown (bottom panel) is the predicted ΔE_{FWHM} as a function of applied magnetic field calculated from the small signal transition parameters and calculated directly from the average measured Mn-Kα x-ray and noise spectral density. The corresponding measured and calculated ΔI and τ_{etf} are presented in (b) for the case of constant $I_{bias} = 382\,\mu$A.

abrupt discontinuous features in α and β with applied field and resistance. Though the model also predicts this type of structure, further study is required to conclusively determine whether these features can be directly correlated to specific features in the critical current. In general the measured α and β values are an order of magnitude smaller than that predicted by the RSJ model (even when accounting for variations due to the I and T dependence to I_C). This may be a result of broadening due to non-equilibrium superconductivity effects or deviations from the sinusoidal current-phase relation assumed in the simple one-dimensional RSJ model, or the effect of non-uniform current density distribution (and the associated self-induced magnetic field from the current). The complex geometry of these devices means that a full microscopic model, including non-equilibrium, weak-link superconductivity, and the role of self-induced magnetic fields, will likely be extremely challenging to develop.

Measurements of the signal responsivity to Mn-Kα x-rays show oscillatory pulse height and decay time consistent with calculations from the small signal transition parameters and illustrate how weak-link physics manifests itself in the detector responsivity. We have also studied the detector noise as a function of field and resistance and have shown that the near-equilibrium expansion of the TES Johnson noise consistently defines a lower limit on the detector bandwidth limiting noise. In addition, small regions of unexplained detector noise have been found around the narrow regions of large α. Measurements suggest there are two régimes of operation—that of $\alpha < \sim 100$, in which there typically seems to be low levels of unexplained noise ($M^2 < \sim 1$) and that of $\alpha > \sim 100$ where M^2 is strongly dependent upon α. The combined effect of the field dependent responsivity and noise result in a complicated field dependence of the predicted energy resolution that makes optimization challenging.

Although it is not yet possible to quantitatively predict $R(T,I,B)$ with complete certainty, these results show how the underlying weak-link physics affects α and β, and ultimately the detector resolution. In order to improve TES energy resolution, there are two obvious routes. Firstly, making devices with large α and no (or at least reduced) unexplained noise, and secondly reducing the near-equilibrium Johnson noise term 2β. The use of interdigitated metal stripes for noise mitigation has been empirically shown to reduce M^2 at the expense of reducing α, consistent with the trend reported here. However it is not clear whether the reduction in noise comes as a result of reducing α or is an independent effect. Furthermore, it is not known whether the additional levels of unexplained noise are associated with higher order Johnson noise terms or from a different physical process all together. The results presented here suggest that by engineering the $I_C(T,B)$ with the use of normal or superconducting metal structures in conjunction with the appropriate field environment (externally applied or self-induced) it may be possible to change $R(T,I,B)$. We are currently in the process of designing and testing devices with different metal features that allow us to vary the superconducting order parameter ψ^2 across the weak-link by means of the proximity effect. By adjusting ψ^2 we can directly change $I_C(T,B)$ and potentially probe a different phase space of $R(T,I,B)$, which may yield different relationships between α, β and potentially M^2, and ultimately may allow us to engineer an "ideal" TES.

ACKNOWLEDGMENTS

This research was in part supported by appointment (C. N. Bailey, S. E. Busch, S. J. Lee) to the NASA Postdoctoral Program at Goddard Space Flight Center, administered by Oak Ridge Associated Universities through a contract with NASA. We thank Jörn Beyer (PTB-Berlin) for providing the SQUIDs used in this work. This material is based upon work supported by the National Aeronautics and Space Administration under an award issued through its Astrophysics Research and Analysis Program.

[1]K. D. Irwin and G. C. Hilton, "Cryogenic particle detection," in *Topics in Applied Physics*, edited by C. Enss (Springer, Berlin, 2005), Vol. 99.
[2]C. A. Kilbourne, "Application of low-temperature detectors to high-resolution X-ray spectroscopy," AIP Conf. Proc. **1185**, 419–425 (2009).
[3]F. Gatti, "Contributions of low temperature detectors to neutrino physics," AIP Conf. Proc. **1185**, 553–557 (2009).
[4]M. W. Rabin, "National and international security applications of cryogenic detectors—Mostly nuclear safeguards," AIP Conf. Proc. **1185**, 725–732 (2009).
[5]P. L. Brink, "Review of dark matter direct detection using cryogenic detectors," J. Low Temp. Phys. **167**, 1048 (2012).
[6]D. A. Bennett, R. D. Horansky, D. R. Schmidt, A. S. Hoover, R. Winkler, B. K. Alpert, J. A. Beall, W. B. Doriese, J. W. Fowler, C. P. Fitzgerald, G. C. Hilton, K. D. Irwin, V. Kotsubo, J. A. B. Mates, G. C. O'Neil, M. W. Rabin, C. D. Reintsema, F. J. Schima, D. S. Swetz, L. R. Vale, and J. N. Ullom, "A high resolution gamma-ray spectrometer based on superconducting microcalorimeters," Rev. Sci. Instrum. **83**, 093113 (2012).
[7]P. Roelfsema, M. Giard, F. Najarro, K. Wafelbakker, W. Jellema, B. Jackson, B. Swinyard, M. Audard, Y. Doi, M. Griffin, F. Helmich, F. Kerschbaum, M. Meyer, D. Naylor, H. Nielsen, G. Olofsson, A. Poglitsch, L. Spinoglio, B. Vandenbussche, K. Isaak, and J. R. Goicoechea, "The SAFARI imaging spectrometer for the SPICA space observatory," in *Proceedings of SPIE 8442, Space Telescopes and Instrumentation 2012: Optical, Infrared, and Millimeter Wave*, edited by M. C. Clampin, G. G. Fazio, H. A. MacEwen, and J. M. Oschmann, Jr. (SPIE, Bellingham, WA, 2012), Vol. 8842, Article No. 84420R.
[8]R. Petre, J. Bregman, M. Bautz, D. Burrows, W. Cash, C. Jones-Forman, S. Murray, P. Plucinsky, B. Ramsey, R. Remillard, C. Wilson-Hodge, A. Ptak, J. Bookbinder, M. Garcia, R. Smith, and G. Daelemans, "The NASA X-ray mission concepts study," in *Proceedings of SPIE, Space Telescopes and Instrumentation 2012: Ultraviolet to Gamma Ray*, edited by T. Takahashi, S. S. Murray, J.-W. A. den Herder (SPIE, Bellingham, WA, 2012), Vol. 8443, Article No. 844317.
[9]R. L. Kelley, S. R. Bandler, W. B. Doriese, Y. Ezoe, R. Fujimoto, L. Gottardi, R. Den Hartog, J.-W. Den Herder, H. Hoevers, K. D. Irwin, Y. Ishisaki, C. A. Kilbourne, P. De Korte, J. Van Der Kuur, K. Mitsuda, T. Ohashi, L. Piro, F. S. Porter, K. Sato, K. Shinozaki, P. Shirron, S. J. Smith, Y. Takei, P. Whitehouse, and N. Y. Yamasaki, "The X-ray microcalorimeter spectrometer for the international X-ray observatory," AIP Conf. Proc. **1185**, 757–760 (2009).
[10]F. S. Porter, P. Beierdorfer, G. Brown, W. Doriese, J. Gygax, R. L. Kelley, C. A. Kilbourne, J. King, K. Irwin, C. Reintsema, and J. Ullom, "The EBIT calorimeter spectrometer: A new, permanent user facility at the LLNL EBIT," J. Low Temp. Phys. **151**, 1061–1066 (2008).
[11]C. A. Kilbourne, W. B. Doriese, S. R. Bandler, R. P. Brekosky, A.-D. Brown, J. A. Chervenak, M. E. Eckart, F. M. Finkbeiner, G. C. Hilton, K. D. Irwin, N. Iyomoto, R. L. Kelley, F. S. Porter, C. D. Reintsema, S. J. Smith, and J. N. Ullom, "Multiplexed readout of uniform arrays of TES x-ray microcalorimeters suitable for Constellation-X," in *Proceedings of the Society of Photo-Optical Instrumentation Engineers (SPIE), Space Telescopes and Instrumentation 2008: Ultraviolet to Gamma Ray*, edited by M. J. L. Turner and K. A. Flanagan (SPIE, Bellingham, WA, 2008), Vol. 7011, Article No. 701104.

[12]M. E. Eckart, J. S. Adams, S. R. Bandler, R. P. Brekosky, A.-D. Brown, J. A. Chervenak, A. J. Ewin, F. M. Finkbeiner, R. L. Kelley, C. A. Kilbourne, F. S. Porter, J. E. Sadleir, S. J. Smith, E. Figueroa-Feliciano, and P. Wikus, "Large-area transition-edge-sensor X-ray microcalorimeters and the micro-X detector array," AIP Conf. Proc. **1185**, 699–702 (2009).
[13]S. J. Smith, J. S. Adams, C. N. Bailey, S. R. Bandler, J. A. Chervenak, M. E. Eckart, F. M. Finkbeiner, R. L. Kelley, C. A. Kilbourne, F. S. Porter, and J. E. Sadleir, "Small pitch transition-edge sensors with broadband high spectral resolution for solar physics," J. Low Temp. Phys. **167**, 168–175 (2012).
[14]J. E. Sadleir, S. J. Smith, S. R. Bandler, J. A. Chervenak, and J. R. Clem, "Longitudinal proximity effect in superconducting transition-edge sensors," Phys. Rev. Lett. **104**, 047003 (2010).
[15]J. E. Sadleir, "Superconducting transition-edge sensor physics," Ph.D. dissertation (University of Illinois, 2010).
[16]J. E. Sadleir, S. J. Smith, I. K. Robinson, F. M. Finkbeiner, J. A. Chervenak, S. R. Bandler, M. E. Eckart, and C. A. Kilbourne, "Proximity effects and non-equilibrium superconductivity in transition-edge sensors," Phys. Rev. B **84**, 184502 (2011).
[17]K. D. Irwin, "Thermodynamics of nonlinear bolometers near equilibrium," Nucl. Instrum. Methods Phys. Res. A **559**, 718–720 (2006).
[18]J. N. Ullom, W. B. Doriese, G. C. Hilton, J. A. Beall, S. Deiker, W. D. Duncan, L. Ferreira, K. D. Irwin, C. D. Reintsema, and L. R. Vale, "Characterization and reduction of unexplained noise in superconducting transition-edge sensors," Appl. Phys. Lett. **84**, 4206–4208 (2004).
[19]N. Iyomoto, S. R. Bandler, R. P. Brekosky, A.-D. Brown, J. A. Chervenak, E. Figueroa-Feliciano, F. M. Finkbeiner, R. L. Kelley, C. A. Kilbourne, M. A. Lindeman, F. S. Porter, T. Saab, J. E. Sadleir, and S. J. Smith, "Modeling of TES X-ray microcalorimeters with a novel absorber design," J. Low Temp. Phys. **151**, 406–412 (2008).
[20]K. K. Likharev, "Superconducting weak-links," Rev. Mod. Phys. **51**, 101–151 (1979).
[21]A. A. Golubov, M. Yu. Kupriyanov, and E. Il'ichev, "The current-phase relation in Josephson junctions," Rev. Mod. Phys. **76**, 411–469 (2004).
[22]A. Kozorezov, A. A. Golubov, D. D. E. Martin, P. A. J. de Korte, M. A. Lindeman, R. A. Hijmering, and J. K. Wigmore, "Microscopic model of a transition-edge sensor weak-link," IEEE Trans. Appl. Supercond. **21**, 250–253 (2011).
[23]A. Barone and G. Paterno, *Physics and Applications of the Josephson Effect* (Wiley & Sons, New York, 1982).
[24]H. A. Notarys and J. E. Mercereau, "Proximity effect bridge and superconducting microcircuitry," J. Appl. Phys. **44**, 1821 (1973).
[25]E. P. Harris, "Properties of superconducting weak links produced by ion implantation," J. Vac. Sci. Technol. **12**, 1383 (1975).
[26]J. Clarke, "Supercurrents in lead-copper-lead sandwiches," Proc. R. Soc. London, Ser. A **308**, 447–471 (1969).
[27]N. Iyomoto, C. A. Kilbourne, S. R. Bandler, R. P. Brekosky, A.-D. Brown, J. A. Chervenak, F. M. Finkbeiner, R. L. Kelley, F. S. Porter, S. J. Smith, J. E. Sadleir, and E. Figueroa-Feliciano, "Close-packed arrays of transition-edge x-ray microcalorimeters with high spectral resolution at 5.9 keV," Appl. Phys. Lett. **92**, 013508 (2008).
[28]M. A. Lindeman, S. Bandler, R. P. Brekosky, J. A. Chervenak, E. Figueroa-Feliciano, F. M. Finkbeiner, T. Saab, and C. K. Stahle, "Characterization and reduction of noise in Mo/Au transition edge sensors," Nucl. Instrum. Methods Phys. Res A **520**, 348–350 (2004).
[29]C. A. Kilbourne, S. R. Bandler, A.-D. Brown, J. A. Chervenak, E. Figueroa-Feliciano, F. M. Finkbeiner, N. Iyomoto, R. L. Kelley, F. S. Porter, and S. J. Smith, "Uniform high spectral resolution demonstrated in arrays of TES x-ray microcalorimeters," in *Proceedings of the Society of Photo-Optical Instrumentation Engineers (SPIE), UV, X-Ray, and Gamma-Ray Space Instrumentation for Astronomy XV*, edited by O. H. W. Siegmund (SPIE, Bellingham, WA, 2007), Vol. 6686, p. 668606.
[30]A. Kozorezov, A. A. Golubov, D. D. E. Martin, P. A. J. de Korte, M. A. Lindeman, R. A. Hijmering, J. van der Kuur, H. F. C. Hoevers, L. Gottardi, M. Y. Kupriyanov, and J. K. Wigmore, "Modelling the resistive state in a transition edge sensor," Appl. Phys. Lett. **99**, 063503 (2011).
[31]W. T. Coffey, Yu. P. Kalmykov, and J. T. Waldron, *The Langevin Equation* (World Scientific, 2004).
[32]M. Tinkham, *Introduction to Superconductivity*, 2nd ed. (Dover Books on Physics, 1996).
[33]K. D. Irwin, G. C. Hilton, D. A. Wollman, and J. M. Martinis, "Thermal-response time of superconducting transition-edge microcalorimeters," J. Appl. Phys. **83**, 3978–3985 (1998).
[34]W. J. Skocpol, M. R. Beasley, and M. Tinkham, "Phase-slip centers and nonequilibrium processes in superconducting tin microbridges," J. Low Temp. Phys. **16**, 145–167 (1974).
[35]D. A. Bennett, D. S. Swetz, R. D. Horansky, D. R. Schmidt, and J. N. Ullom, "A two-fluid model for the transition shape in transition-edge sensors," J. Low Temp. Phys. **167**, 102–107 (2012).
[36]T. S. Wang, G. C. Guo, Q. F. Zhu, J. X. Wang, T. F. Li, J. S. Liu, W. Chen, and X. X. Zhou, "Device modeling of superconductor transition-edge sensors based on the two-fluid theory," IEEE Trans. Appl. Supercond. **22**, 2100212 (2012).
[37]V. Ambegaokar and B. I. Halperin, "Voltage due to thermal noise in the dc Josephson effect," Phys. Rev. Lett. **22**, 1364–1366 (1969).
[38]J. E. Sadleir, S. J. Smith, S. R. Bandler, J. S. Adams, S. E. Busch, M. E. Eckart, J. A. Chevenak, R. L. Kelley, C. A. Kilbourne, F. S. Porter, J.-P. Porst, and J. R. Clem, "Magnetically tuned superconducting transition-edge sensors," IEEE Trans. Appl. Supercond. **23**, 2101405 (2013).
[39]M. A. Lindeman, S. R. Bandler, R. P. Brekosky, J. Chervenak, E. Figueroa-Feliciano, F. Finkbeiner, M. J. Li, and C. A. Kilbourne, "Impedance measurements and modeling of a transition-edge-sensor calorimeter," Rev. Sci. Instrum. **75**, 1283–1289 (2004).
[40]C. H. Whitford, W. M. Bergmann Tiest, and A. D. Holland, "Practical considerations in optimal filtering of TES signals," Nucl. Instrum. Methods Phys. Res. A **520**, 592–594 (2004).
[41]N. Jethava, J. N. Ullom, K. D. Irwin, W. B. Doriese, J. A. Beall, G. C. Hilton, L. R. Vale, and B. Zink, "Dependence of excess noise on the partial derivatives of resistance in superconducting transition edge sensors," AIP Conf. Proc. **1185**, 31–33 (2009).
[42]K. M. Kinnunen, M. R. J. Palosaari, and I. J. Maasilta, "Normal metal-superconductor decoupling as a source of thermal fluctuation noise in transition-edge sensors," J. Appl. Phys. **112**, 034515 (2012).